Icarus 364 (2021) 114480

Contents lists available at ScienceDirect

Icarus

journal homepage: www.elsevier.com/locate/icarus

Geology of the Chang'e-5 landing site: Constraints on the sources of samples returned from a young nearside mare

Le Qiao [a,*], Jian Chen [a], Luyuan Xu [b,c], Sheng Wan [a], Haijun Cao [a], Bo Li [a], Zongcheng Ling [a]

[a] Shandong Key Laboratory of Optical Astronomy and Solar-Terrestrial Environment, School of Space Science and Physics, Institute of Space Sciences, Shandong University, Weihai, Shandong 264209, China.
[b] State Key Laboratory of Lunar and Planetary Sciences, Macau University of Science and Technology, Macau, China
[c] CNSA, Macau Center for Space Exploration and Science, Macau, China

ARTICLE INFO

Keywords:
Chang'e-5
Lunar landing site
Sample return mission
Young mare basalts
Oceanus Procellarum

ABSTRACT

Extraterrestrial materials collected by sample return exploration missions have advanced our understanding of planetary formation and evolution in a profound manner. This is achieved through sophisticated laboratory sample analyses with very high precision and accuracy that are difficult to obtained by orbital or surface landing/roving explorations. Moreover, the well-known geographical location and geological context of returned samples enable the sample measurements to be fully interpreted and mapped into the entire planetary context (in contrast to meteorites where the geological context is missing). Planetary scientists have been endeavoring to collect and returned samples from extraterrestrial bodies, despite the significant costs involved.

In December 2020, China's Chang'e-5 mission successfully landed in and returned lunar samples from the northeastern Oceanus Procellarum in the western lunar nearside maria. The mare basalt at the landing site has been dated to be ~1–2 Ga through crater population studies, much younger than any basalts in the present lunar sample collections and among the youngest maria on the global Moon (e.g., Hiesinger et al., 2011). The Chang'e-5 sample will provide an unprecedented opportunity to characterize the late-stage lunar volcanism.

To fully explore the scientific potential of the Chang'e-5 returned samples and assist the on-going sample analyses and interpretations, we present an in-depth investigation of the geology of the specific Chang'e-5 landing site and the nearby vicinity using high-resolution remote sensing data sets. We characterize the detailed geological context, topography, morphology, morphometry, chemical and mineralogical composition of the local landing area. These geological characterizations lead us to identify a sequence of four geological events, including mare volcanism, tectonism, impact cratering and ejecta deposition, that have potentially affected and been recorded in the returned samples. Compositional and geochronological measurements of the Chang'e-5 samples would reconstruct a detailed regional geological evolution model of the landing area. Furthermore, most of the inferred ages of these geological events lie in the age gap of the Apollo/Luna samples. Precise determination of these ages through radiogenic isotope analyses would be invaluable in narrowing down the uncertainties of the lunar cratering chronology function and improve our understanding of the geological history of the entire Moon.

1. The Chang'e-5 mission: returning samples from the western nearside young maria

Sample return missions are among the most advanced scientific exploration modes of extraterrestrial worlds. The key advantage of sample return missions is to enable sophisticated laboratory analyses of the returned planetary materials by the state-of-the-art instruments on the Earth. These high-precision and highly accurate measurements are essential for assessing the scientific gaps remained from earlier-phase remote sensing and landed explorations. Most importantly, returned samples are also "the gifts that keeps on giving" as they can be carefully preserved for decades and analyzed in the future to explore scientific questions that have not been formulated using instruments and technologies that do not exist currently (Anand et al., 2020).

Meteorites are another type of extraterrestrial samples that can be precisely analyzed in laboratory facilities and have been invaluable in

* Corresponding author.
E-mail address: leqiao.geo@gmail.com (L. Qiao).

https://doi.org/10.1016/j.icarus.2021.114480
Received 5 February 2021; Received in revised form 14 April 2021; Accepted 14 April 2021
Available online 18 April 2021
0019-1035/© 2021 Elsevier Inc. All rights reserved.

advancing our understanding of the planetary formation and evolution. For instance, the oldest and youngest mare basalts identified to date are both from lunar meteorites (e.g., Terada et al., 2007; Borg et al., 2004; Snape et al., 2018). Nevertheless, without precise information on the geographical provenance and geological context, many meteorite measurements cannot be fully interpreted and mapped into the entire planetary context. Returned samples have this unique benefit for their well-known geographic and geological context, and have yielded significant insights into our solar system in a profound manner. In addition, returned samples can be sealed under the primitive environments of their parent bodies and are free of contamination by the terrestrial environment. This can clarify many disputes concerning the analysis results, which are very helpful for the full and reliable scientific interpretations. Furthermore, these returned samples also provide critically important "ground truth" for verifying and calibrating remote-sensed measurements. These claims have been amply demonstrated by the lunar samples returned by the United States Apollo and Soviet Luna missions, which have basically transformed our understanding of the solar system (e.g., LSPET, 1970; Vinogradov, 1971; Bence et al., 1972; Lawrence and Neal, 2019; Zeigler et al., 2019). Planetary scientists have been endeavoring to collect samples from extraterrestrial bodies, despite the significant costs involved and the availability of many meteorites delivered from outer space to the Earth.

The Moon remains as the only planetary body other than the Earth for which samples have been collected from well-known places on regional geological units by the very successful Apollo and Luna missions. These precious samples have fundamentally revolutionized our knowledges on the origin and evolution of the Moon, and continue doing so. Notwithstanding all this, the surface geological units represented by the Apollo/Luna landing sites comprise far less than half the lunar surface. All the Apollo and Luna samples were collected from regions near to the nearside lunar equator. The entire lunar farside and polar regions remain unsampled. Subsequent remote sensing data from orbital spacecraft revealed that the Apollo/Luna landing sites were all located in a compositionally anomalous province of the Moon and heavily affected by a small number of large impact basins (Imbrium and Serenitatis). Moreover, the existing returned lunar samples do not represent the wide range of compositional and chronological characteristics of lunar surface. For instance, no geological events either $> \sim$ 3.9 or $\sim$ 1–3 Ga old that tied to surface geologic units has been identified in the Apollo/Luna sample collections (Stöffler and Ryder, 2001). New samples returned from the Moon are urgently needed to address key scientific questions remaining from earlier sampling and remote sensing explorations (Head, 2020). China's Chang'e-5 is just such a long-waited sample return mission.

On 1 December 2020 (UTC), the China National Space Administration (CNSA) Chang'e-5 spacecraft successfully landed in and collected lunar samples from the northeastern region of the Oceanus Procellarum on the western lunar nearside maria, and returned the samples to the Earth on 16 December 2020. This is the first lunar sample return mission since the Soviet Luna 24 returned sample from Mare Crisium in the eastern lunar nearside in 1976, 44 years ago. The Chang'e-5 samples are also the largest extraterrestrial samples (1.7 kg) returned to the Earth since the United States Apollo 17 in 1972. The scientific objectives of the Chang'e-5 mission include determining the cessation time of lunar volcanism, assessing the composition of lunar late-state volcanism, and providing an insight into lunar thermal and interior evolution (Li et al., 2019).

The coordinate of the Chang'e-5 landing site is computed to be 43.0576°N, 308.0839°E by the Lunar Reconnaissance Orbiter Camera (LROC) team from the direct LROC imaging of Chang'e-5 lander on lunar surface (LROC, http://lroc.sese.asu.edu/posts/1172). The landing site is located in a broad, flat mare basalt unit, which has been dated through crater population study to be ~1–2 Ga old (Hiesinger et al., 2003; Morota et al., 2011; Qian et al., 2018; 2021a, 2021b; Wu et al., 2018; Jia et al., 2020), much younger than all basalts in the present lunar sample collections (including lunar meteorites) and indeed among the youngest mare basalts on the global Moon. New samples returned by the Chang'e-5 mission will have tremendous potential for an in-depth insight into the origin and evolution of the Moon. The detailed landing site selection procedure can be found in Liu et al. (2020).

In order to fully explore the advantages of lunar sample return missions, it is critically important to have a comprehensive knowledge of landing site geology. Extensive geological studies of the Moon over the past decades have shown that any small part of the lunar surface, even the topographically very flat mare plains, could be complicated in regional geology. Furthermore, materials deposited on lunar surface are exposed to the continuous meteoritic impact flux, thus subject to impact cratering modifications on-site and contaminations by foreign materials ejected from distant large impacts. Mixing of distant ejecta materials in the returned Chang'e-5 samples would, on the one hand, complicate the samples analyses and scientific interpretations, while on the other hand, enhance the characteristic diversity of the returned samples and provide serendipitous (and sometimes critically important) scientific opportunities. For instance, it was generally accepted that the Apollo 12 mission has collected ray materials from the Copernicus crater approximately 400 km north of the landing site and the Apollo 17 mission has collected landslide materials triggered by ejecta from the Tycho crater over 2200 km southwest of the landing site (Stöffler and Ryder, 2001). These foreign materials in the Apollo 12 and 17 samples have been invaluable in establishing the lunar stratigraphy system and cratering chronology function, seminal scientific achievements for lunar and planetary science. Detailed geological context analyses of sample return mission landing sites will provide critically important and instructive framework for interpreting the sample analysis results in a wider picture of the global lunar geology.

In this contribution, we build on prior large-scale geological studies of the Chang'e-5 landing area in northern Oceanus Procellarum (Zhao et al., 2017; Qian et al., 2018, 2020; 2021a, 2021b; Wu et al., 2018; Yue et al., 2019; Jia et al., 2020; Meng et al., 2020; Xie et al., 2020), and present an in-depth investigation of the geology of the Chang'e-5 landing site and the local vicinity (a 20 × 20 km area surrounding the landing site). We characterize (1) the specific geographical location and geological context, (2) detailed and comprehensive topography, morphology and morphometry, and (3) chemical and mineralogical composition of the landing area and surroundings. These observational analyses lead us to identify a sequence of geological events and their ages that are potentially recorded in the returned Chang'e-5 samples. We analyze the landing site and vicinity using very-high-resolution remote-sensing data sets (pixel dimensions as small as ~1 m) which reveal many details that were otherwise missed in previous large-scale landing site descriptions (Zhao et al., 2017; Qian et al., 2018, 2020; Qian et al., 2021a, 2021b; Wu et al., 2018; Yue et al., 2019; Jia et al., 2020; Meng et al., 2020; Xie et al., 2020). Our results will provide very timely and instructive references for the on-going Chang'e-5 sample analyses and scientific interpretations.

2. Data and methodology

We first characterize the geographical location and geological setting of the Chang'e-5 landing site, including the context of the northern Oceanus Procellarum, the mare units at the landing site and the local vicinity, using the latest moderate-resolution orbital images from the Lunar Reconnaissance Orbiter (LRO) Wide-Angle Camera (LROC WAC, 100 m/pixel, Robinson et al., 2010) and Kaguya/SELENE Terrain Camera (TC, 10 m pixel size, Haruyama et al., 2008), and altimetric data sets from LRO Lunar Orbiter Laser Altimeter (LOLA, 128 pixel/degree spatial sampling and ~ 10 cm vertical altimetric accuracy, Smith et al., 2010) and LOLA + TC merged topography (SLDEM2015, 512 pixels/degree spatial sampling and ~ 3–4 m ranging precision, Barker et al., 2016). We then analyze the detailed topography, slope, morphology, and morphometry of the Chang'e-5 landing site and the nearby vicinity

using topography data sets from raw LRO LOLA laser altimetric measurements and Kaguya TC photogrammetry digital terrain model (DTM, 10 m pixel size and ~ 3–4 m altimetric accuracy; Haruyama et al., 2012), and high-resolution images from LROC Narrow-Angle Camera images (LROC NAC, 1.11–1.63 m/pixel, Robinson et al., 2010) and the Landing Camera aboard the Chang'e-5 lander (LCAM, centimeter-scale). Each individual LROC NAC image is produced from raw EDR (experiment data record) data through routine process sequences using the USGS Integrated Software for Imagers and Spectrometers (ISIS3; Anderson et al., 2004). We also characterize the FeO and TiO_2 contents across the landing area from Kaguya Multiband Imager (MI) reflectance maps using algorithms of Lemelin et al. (2015) and Otake et al. (2012), respectively. The errors for the MI-derived FeO and TiO_2 content are 0.43 wt% (weight percentage) and ~ 1 wt% relative to compositions of the returned Apollo/Luna samples. Finally, we investigate the mineralogical composition of the mare surface surrounding the Chang'e-5 landing site using Chandrayaan-1 Moon Mineralogy Mapper (M^3) imaging spectrometer data collected during the optical period (OP) 2C (280 m/pixel, Boardman et al., 2011). Three tie points at fixed wavelengths (700, 1579, and 2500 nm) were used to define a two-part linear continuum and remove the continuum of the M^3 reflectance spectra. Integrated band depths (IBD) of absorption features at 1 and 2 μm (IBD1000 and IBD2000) are calculated from the M^3 scenes to capture the mafic mineral diversity of the landing area surface. We also determinate spectral parameters including absorption band centers at 1 and 2 μm by 4th order polynomial fitting and the IBD2000/IBD1000 ratio (IBDR) for

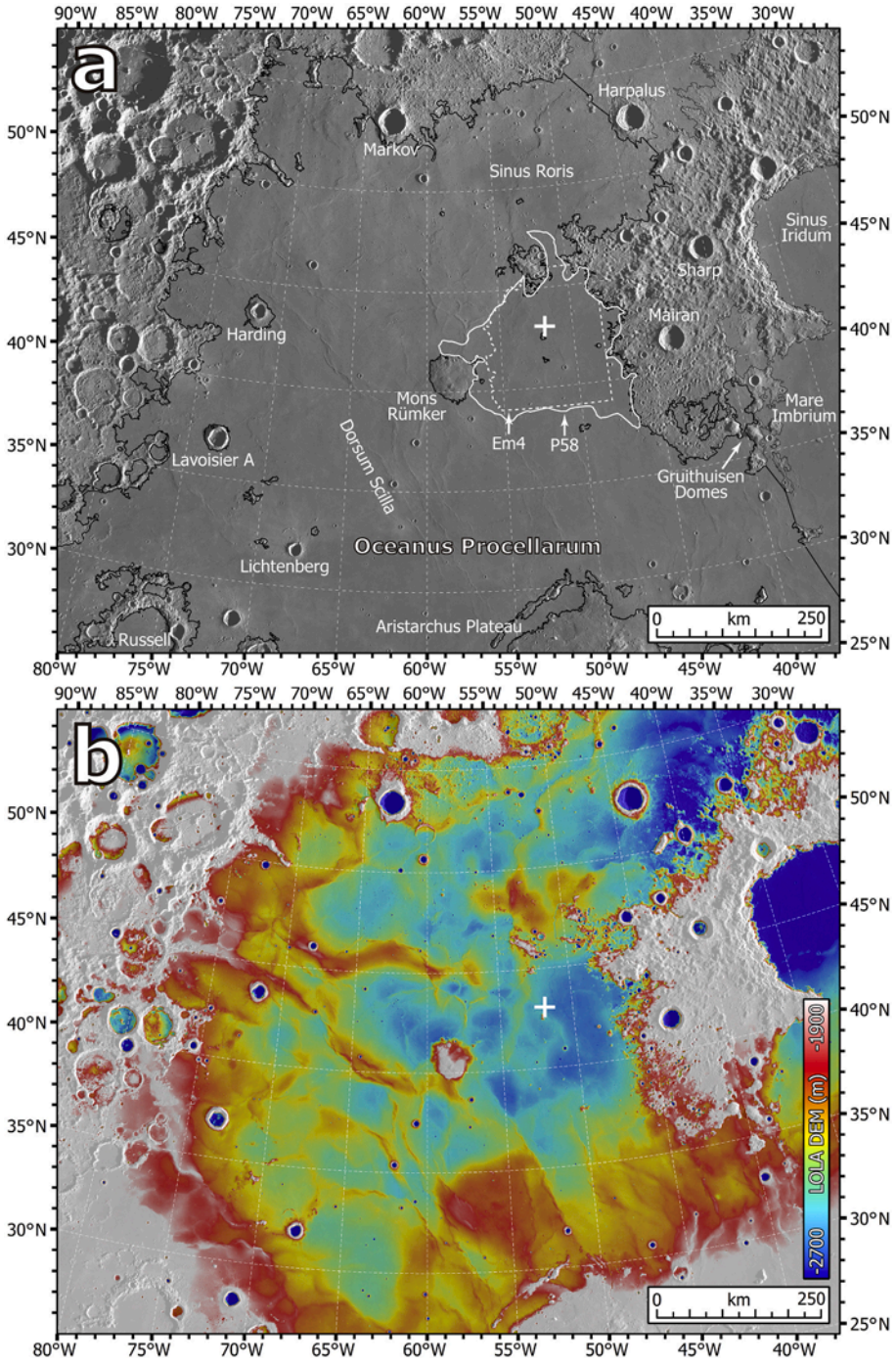


Fig. 1. (a) Major physiographic features within the regional context of Chang'e-5 landing site in the northern Oceanus Procellarum. The Chang'e-5 site is indicated by the white cross, the boundaries of P58 (Hiesinger et al., 2003) and Em4 (Qian et al., 2018) mare units are delineated by bold and dashed white polygons, respectively. The bold black polygons indicate the boundaries of mare deposits in Oceauns Procellarum and the thinner black polygons for maria elsewhere. The background image is a portion of the LROC WAC nearside low-sun mosaic (100 m/pixel). (b) LOLA DEM topography (128 pixel/degree) overlaid on LROC WAC mosaic. The projection is Lambert conformal conic projection, centered at 40°N, 60°W, and north is toward the top.

M^3 spectra collected from fresh sub-kilometer craters to characterize the composition and relative abundance of mafic minerals (Ling et al., 2019 and reference therein for the M^3 data process).

3. Geologic context of Chang'e-5 sampling site

The Chang'e-5 lander/ascender combination successfully landed in and collected lunar materials with a drill and scoop sampling equipment from a flat mare surface in the northeastern Oceanus Procellarum of the western nearside of the Moon (Fig. 1). Oceanus Procellarum is the largest mare on the Moon and the only mare being called as "Oceanus" (Latin for "ocean"), presciently showing its uniqueness in lunar studies. The western nearside of the Moon, mainly composed of Oceanus Procellarum and western Mare Imbrium, was historically known as the site of the last major phase of lunar volcanism (e.g., Boyce, 1976; Schultz et al., 1976). Crater morphology and population dating analyses from orbital images revealed that many of these mare deposits were even younger than the Apollo 12 low-Ti basalts (Boyce, 1976; Schultz and Spudis, 1983; Hiesinger et al., 2003, 2011a), the youngest returned mare basalts and radioisotopically-dated as young as 3.1 Ga (Snyder et al., 1997; Snape et al., 2018). The youngest surface mare basalt units, all found within Oceanus Procellarum from imaging data, were suggested to be erupted ~0.9–1.5 Ga ago (Schultz and Spudis, 1983; Hiesinger et al., 2011a; Morota et al., 2011), which significantly prolonged the lifetime of lunar mare volcanism previously established by return sample isotopic dating analyses (e.g., Papike et al., 1976). The late-stage mare basalts emplaced in lunar western nearside are also distinct for its unique spectroscopic and thus compositional characteristics. Earlier telescopic spectra measurements identified very high ultraviolet/visible spectral ratios for these basalts, suggesting a very high titanium abundance (e.g., Charette et al., 1974; Pieters, 1978). Subsequent acquisition of high-resolution orbital multispectral data of lunar surface enabled the establishment of empirical relationships between remote-sensed spectral data and returned sample composition. The resultant titanium content map of the global Moon supported the interpretation of titanium-rich nature for these late-stage basalts (e.g., Lucey et al., 1998; Sato et al., 2017). The latest lunar mare titanium abundance mapping effort using repeated LROC WAC spectral observations reported a maximum TiO_2 content of 11.7 wt% for Oceanus Procellarum basalts, indeed among the most titanium-rich basalts on the Moon (Sato et al., 2017). Spectroscopic studies further revealed that the western nearside basalts exhibit a relatively strong 1 μm absorption band, while a very weak to nearly absent 2 μm absorption band, suggesting a unique olivine-rich composition (e.g., Pieters, 1978; Staid et al., 2011; Varatharajan et al., 2014).

The Chang'e-5 sampling site is just located in one of the youngest mare units on the Moon. Hiesinger et al. (2003) defined a spectrally homogeneous mare unit for the basaltic deposits surrounding the Chang'e-5 site using Clementine multispectral images and denoted it the "P58" mare unit (Fig. 1; P for Oceanus Procellarum and the numbering 58 indicates the 58th oldest age among the 60 mare units in Oceanus Procellarum, implying the third youngest one). Hiesinger et al. (2003) dated this P58 mare unit as 1.33 (+0.19/−0.25) Ga from crater population analysis on Lunar Orbiter IV images (60–150 m/pixel). Morota et al., (2011) conducted an updated crater counting dating analysis of the P58 mare unit using Kaguya TC images obtained at a spatial resolution of 10 m/pixel and under low-Sun illuminations, and derived a model age of 1.91 (±0.11) Ga (this work also proposed an alternative age of 2.20 ± 0.13 Ga using a different lunar crater production and chronology function; Table S1). The thickness of the basalt unit at the Chang'e-5 sampling site is estimated to be <40 m from crater excavation method (Qian et al., 2021a).

After the target landing area of Chang'e-5 in northern Oceanus Procellarum (41–45°N, 49–69°W) was declared, five studies performed independent crater counting and age dating analyses for the mare deposits at the Chang'e-5 landing area, and reported different dating results (Table S1): 1.21 (±0.03) Ga (Qian et al., 2018), 1.49 (±0.17) Ga (Wu et al., 2018), 2.07 (+0.026/−0.027) Ga (Jia et al., 2020), 1.53 (±0.027) Ga (Qian et al., 2021a), and 1.60 (±0.16) Ga (Qian et al., 2021b). (Note that these five studies all worked on the Eratosthenian-aged mare unit Em4 surrounding the Chang'e-5 site defined by Qian et al. (2018) using Kaguya MI spectral and compositional maps (Fig. 1), which broadly overlaps with the P58 mare unit, though their crater counting areas are different from each other.) The range of ages derived from the same lunar surface area from different studies (1.2–2.2 Ga) is likely attributed to the variations in the employed imaging data (resolution and illumination condition), crater count working area (location and size), diameter range and numbers of craters for age calculation, crater counting method (manual or automatic), lunar crater production and chronology functions (Table S1), and measurement variations between different investigators (Robbins et al., 2014), but also reveals the many challenges and uncertainties in inferring absolute ages from crater population studies. Nonetheless, these ages are all much younger than any lunar basalts in the present lunar sample collections and lie in the age gap of calibration points of the lunar chronology function (~0.8–3.1 Ga, Stöffler and Ryder, 2001). Accurate isotopic dating results of the basalts collected by Chang'e-5 will provide critically important data for calibrating the lunar impact flux and chronology function, which is also the basis for the chronology of all the terrestrial planets.

Regionally, the P58 mare basalt unit at the Chang'e-5 site is located at the northeastern margin of the Oceanus Procellarum, adjacent to the highly cratered ejecta deposits west of the 249-km-diameter Iridum crater (e.g., Qiao et al., 2014). The Chang'e-5 sampling site is ~80 km from the edge of the Iridum ejecta blanket (Figs. 1 and 2). At the southwestern border of the P58 mare unit, Mons Rümker, a huge volcanic dome-flow complex, comprises a lava plateau with an area of ~4000 km^2 (Fig. 1; Zhao et al., 2017). The Rümker plateau is ~80 km in diameter and stands up to ~1300 m from the surrounding mare plain. Over 20 volcanic domes, ranging ~2–14 km in diameter, have been identified on the Mons Rümker (Zhao et al., 2017). Mons Rümker is also one of three major volcanic complexes long recognized in the central Oceanus Procellarum (e.g., Whitford-Stark and Head, 1977). The Chang'e-5 sampling site lies ~105 km northeast of the Mons Rümker (Fig. 1). Numerous wrinkle ridge features occur in the P58 and the adjacent mare units (Figs. 1 and 2). Most of these ridges in the 200 km vicinity of the Chang'e-5 landing site have preferred north-south, northwest-southeast, and northeast-southwest orientations, while dozens of ridges, especially in the eastern mare, are east-west-oriented (Fig. 2). Mare wrinkle ridges are generally interpreted as tectonically contractional structures, while the specific formation mechanism and the cause of stress are not well understood and appear to be complex (Watters and Johnson, 2010). A north-south-oriented wrinkle ridge, measured ~20 km in length, lies just ~2 km west of the Chang'e-5 landing site (Fig. 2).

Several islands of pre-mare highland materials occur within and in the vicinity of the P58 mare unit (Fig. 2). These raised terrains are termed as highland "kipukas" or "steptoes", interpreted as remnants of highland materials that have been surrounded by subsequent lava flows (e.g., Head, 1976a). A prominent group of such highland kipukas occurs in the northern border of the P58 mare unit. The major component of this kipuka group, located between craters Louville D and P, is 65 × 35 km in dimension and stands ~800 m from the surrounding mare surface.

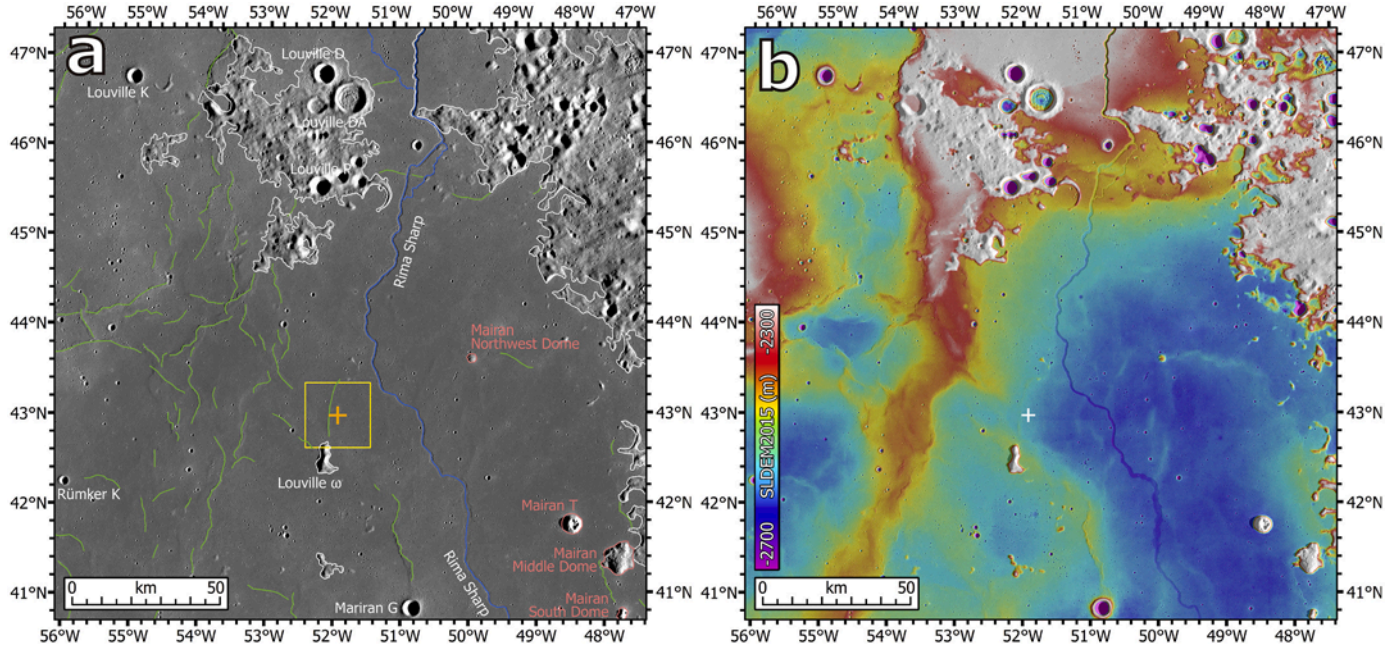


Fig. 2. (a) Regional 200 × 200 km vicinity of the Chang'e-5 landing site: (a) Kaguya TC morning image mosaic (10 m/pixel) and (b) SLDEM2015 (512 pixels/degree) topography overlain on Kaguya TC image. In panel a, the orange cross denotes the landing site of Chang'e-5, the yellow square marks the studied 20 × 20 km landing area (section 4). The blue and green curves indicate sinuous rilles and wrinkle ridges, respectively. A line of four steep Mairan domes are marked by pink polygons. Note that Louville ω, Mairan Northwest/Middle/South domes are not IAU (International Astronomical Union) official names. All maps for the local areas surrounding the Chang'e-5 landing site are projected into Lambert conformal conic projection, centered at 43.1°N, 51.8°W, and north is toward the top, unless otherwise specified. (For interpretation of the references to color in this figure legend, the reader is referred to the web version of this article.)

Another conspicuous kipuka feature, informally named Louville ω in a Lunar Chart (LAC) Series map (LAC-23 Rümker; ACIC, 1967), lies 10 km south of the Chang'e-5 landing site. This kipuka is 10 × 7 km in size at its base and rises ~520 m from the surrounding mare surface. Cameras aboard the Chang'e-5 lander have also imaged this distinct hilly feature in the horizon (Fig. S1). Another group of non-mare features is a line of four steep-sided domes described as Mairan domes, occurring near to the shores of the northeastern Oceanus Procellarum and arranged in a northweast-southeast direction (Fig. 2). These topographically and spectroscopically distinctive domical features have been attributed to localized eruption of unusually silica-rich and viscous magma on the Moon (e.g., Head and McCord, 1978; Glotch et al., 2011).

The 50 × 30 km mare surface surrounding the Chang'e-5 landing site is relatively homogeneous in surface morphology and textures, mainly characterized by small impact craters superposed on basaltic lava plain (Fig. 3). Other than the Louville ω highland kipuka at the south of landing site, two major geological features are present: a segment of the sinuous rille Rima Sharp in the east and a wrinkle ridge ~2 km west of the landing site.

Rima Sharp is designated as the longest sinuous rille among over 200 sinuous rilles catalogued on the Moon, with a length of 566 km (Hurwitz et al., 2013). Rima Sharp is observed to have an average width of 840 m, an average depth of 76 m (1σ = 82 m), a sinuosity of 1.15, and a north-south flow direction (Hurwitz et al., 2013). The rille segment of Rima Sharp in the vicinity of Chang'e-5 landing site is relatively uniform in rille width (0.9–1.0 km) and depth (30–40 m) (Fig. 3). The Chang'e-5 landing site is ~17 km from the edge of Rima Sharp. Sinuous rilles are generally interpreted to represent very high-effusion rate ($>10^4$–10^5 m^3/s) and long-duration volcanic eruptions on the Moon (Head and Wilson, 2017). Being very near from the largest sinuous rilles on the Moon, the lava flows which formed the Rima Sharp may source the mare deposits at the Chang'e-5 sampling site.

The 20-km-long ridge west of Chang'e-5 landing site appears to be generally linear or slightly arc-shaped in outline (Fig. 3). This ridge is ~1–2 km wide, and the southmost segment is somewhat wider. The Chang'e-5 landing site is 2.2 km from the east foot of this ridge. The middle ~4.5 km-long segment of this ridge is relatively subdued in topographical relief: the middle ridge segment is generally ~10–15 m higher than the surrounding mare, while the ridge segments in the south and north rise up to ~25 m. Previous geological studies have mapped out the south ridge segment, while have not identified the subtle middle segment directly west of the landing site (e.g., Qian et al., 2021b). An elevation offset with a relief of ~5–10 m is observed from the two sides of this mare ridge (Fig. 3). Similar elevation offsets have also been observed across many mare ridges (e.g., Golombek et al., 1991), and are attributed to deeply rooted thrust faults or artifacts of regional slope (Golombek et al., 1991; Sharpton, 1992). In the case of the small ridge west of Chang'e-5 site, the latter interpretation is more likely, as this ridge is superposed on a long-wavelength west-east sloping topography of regional surface, which is probably induced by the many large and early-formed ridges in the west (Fig. 2). No clear geomorphological evidence of mare flow ponding, flooding, or buckling against the ridge features is observed, even in very low-Sun LROC WAC images (<10°). It is possible that this wrinkle ridge postdated the emplacement of the nearby mare flows, potentially due to mare loading-induced regional stress.

4. Geological characteristics of the Chang'e-5 landing area

We then turn to the very local 20 × 20 km area surrounding the Chang'e-5 landing site. We investigate its detailed topography, morphology, and quantitative chemical and mineralogical composition using the latest high-resolution orbital observations.

4.1. Topography and slope of the Chang'e-5 landing area

We first refer to the raw LOLA laser range and inferred surface topography measurement spots (also known as "shots") to analyze the topography variations of the landing area, as LOLA original altimetric measurements (without spatial interpolations) provide an

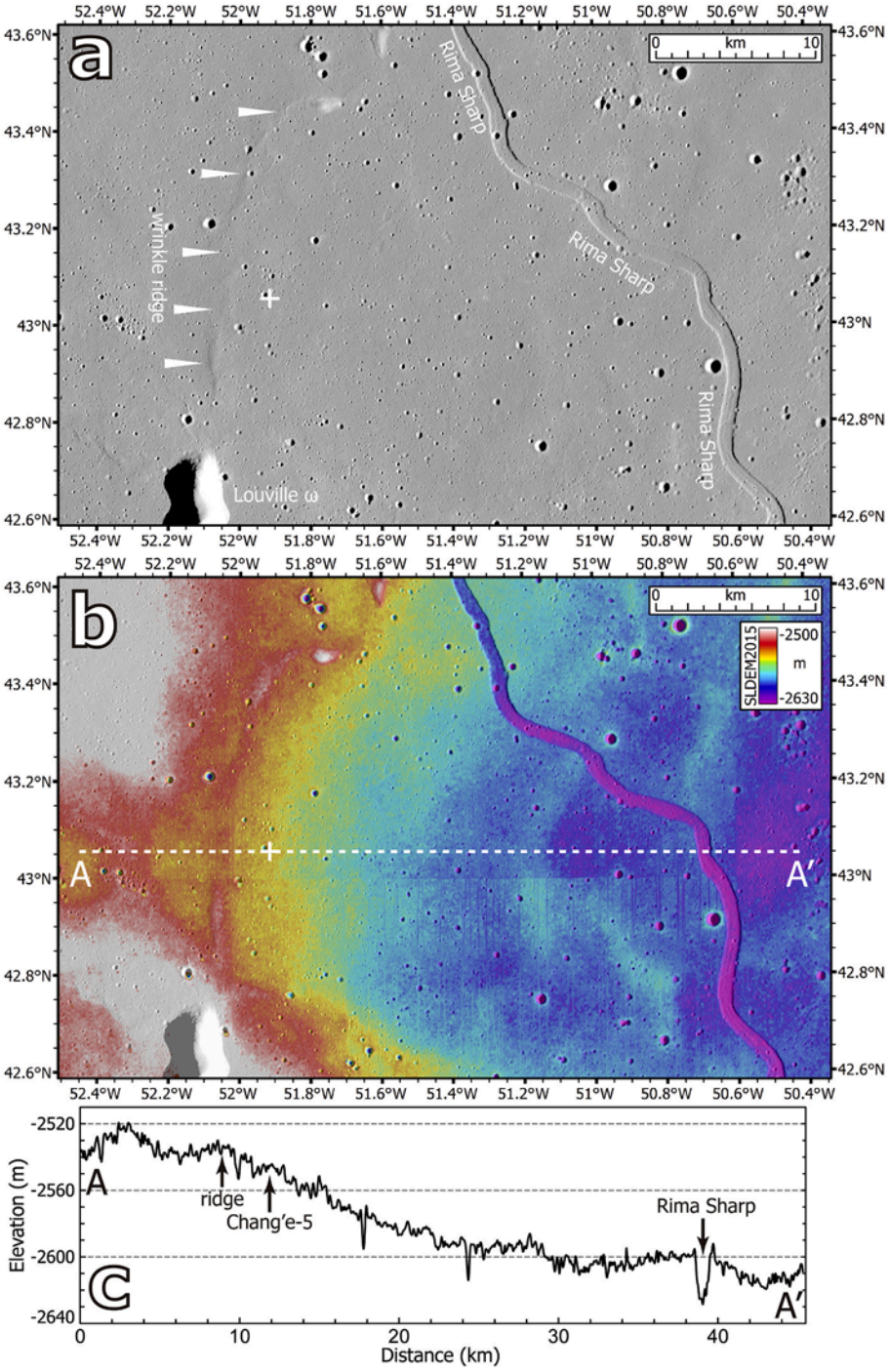


Fig. 3. The local 50 × 30 km area surrounding the Chang'e-5 landing site (marked by the white crosses): (a) Kaguya TC morning image mosaic, (b) SLDEM2015 topography overlain on Kaguya TC image, and (c) a west-east topographical profile across the landing site derived from SLDEM2015 topography (with its location shown as the white dashed line in panel b).

unprecedented ranging precision of ~10 cm, the most precise one among several altimetric data sets of the lunar surface (Smith et al., 2010). During the Primary and Science Missions of LRO during 2009 and 2011, LOLA has collected over 40,000 spot measurements across the 20 × 20 km landing area (Fig. S2a). The surface elevation of the local landing area ranges from about −2630 m to about −2410 m relative to a mean lunar radius of 1737.4 km, with a topographical relief of ~220 m (Fig. S2b), while the majority of the LOLA shots within the 20 × 20 landing area (98.6%) have inferred surface elevations between −2590 m and − 2480 m (Fig. S2b). A general west-east sloping trend is observed across the landing area (Fig. S2a), with an elevation offset of ~60 m. This elevation offset has been seen in the lower-resolution SLDEM2015 topography (Fig. 3b) and is attributed to the regional long-wavelength topographical trend introduced by the large ridges features in the west maria (Fig. 2b). The northwestern and southwestern corners are characterized by relatively higher elevations, which are mare ridges and the Louville ω highland kipuka rising from the maria. The nearest LOLA altimetric measurement spot to the Chang'e-5 landing site, at a distance of ~280 m, has an elevation of −2542.1 m (Fig. S2a).

Due to the polar orbit configuration of the LRO spacecraft, spatial

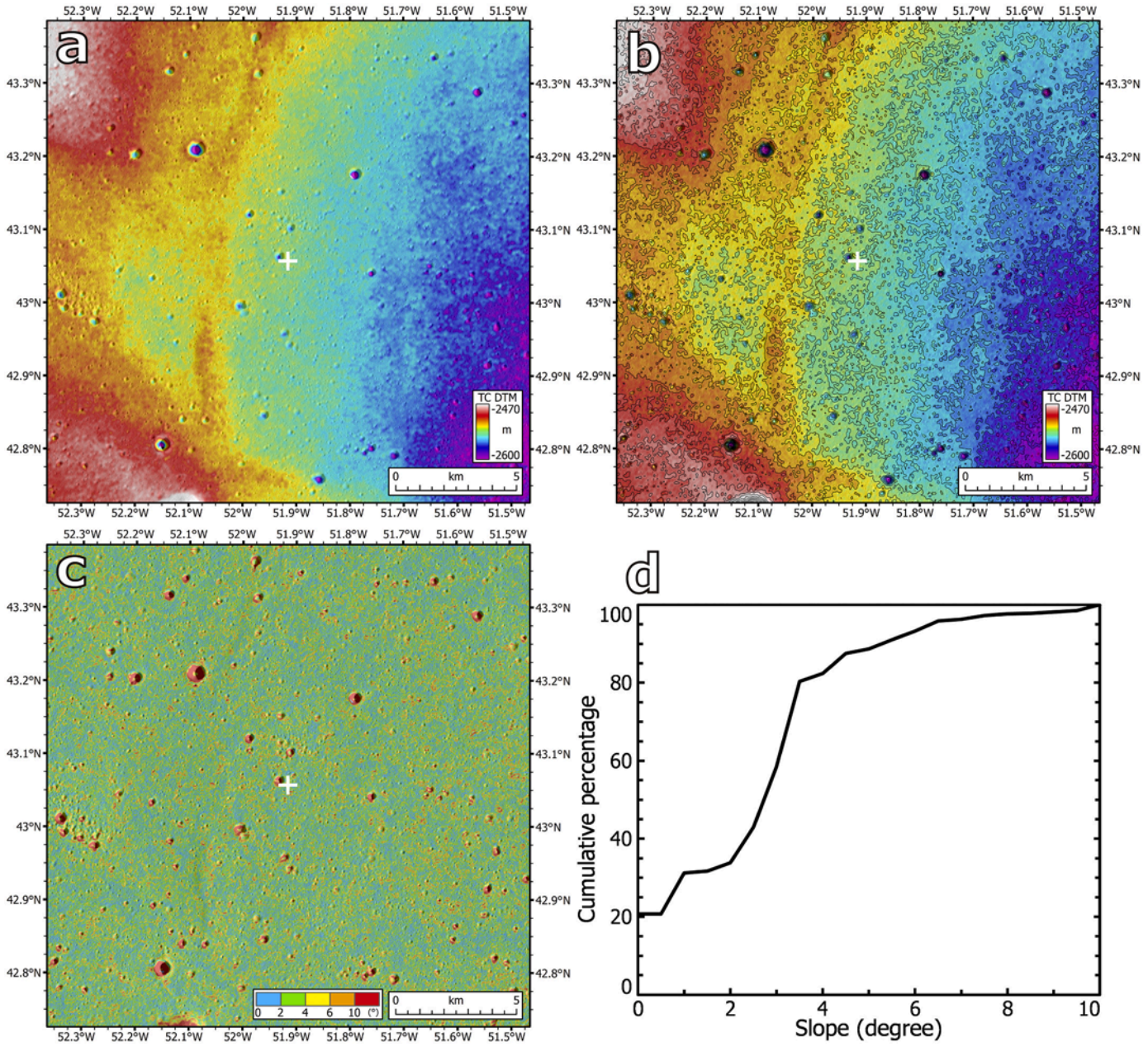


Fig. 4. Kaguya TC topography and slope maps of the Chang'e-5 landing area: (a) TC seamless DTM topography (10 m pixel size) overlain on TC morning mosaic image, (b) 10 m contours derived from TC DTM overlain on panel a, (c) map of TC DTM-derived slope (30 m baseline) overlain TC morning mosaic, and (d) cumulative percentage distribution of topographical slopes with 0.5° interval. The white crosses denote the Chang'e-5 landing site.

sampling gaps as wide as a few kilometers still persist in equatorial and middle-latitude regions for LOLA shot measurement. Fortunately, high-resolution photogrammetry topography obtained by orbital stereo cameras provides much denser surface coverage. We here refer to the Kaguya TC stereogrammetry seamless DTM to characterize the topography and slope of the 20 × 20 km landing area, which provide a uniform spatial sampling of 10 m/pixel of the entire studied area and an excellent altimetric precision of ~3 m (Haruyama et al., 2012). The photogrammetry altimetric mapping results of Kaguya TC DTM across the Chang'e-5 landing area (Figs. 4a, b) generally mimic that of the LOLA original point elevation measurements (Fig. S2a), while provide better representations of topography for many small geological features. From the color-coded map of the Kaguya TC DTM topography, the regional west-east sloping trend and apparent topographical relief of the small ridges west of the landing site, the huge ridges in the northwestern and southwestern corners and the Louville ω kipuka are clearly observed. The Kaguya TC photogrammetry altimetric measurements derive a − 2552 m surface elevation for the Chang'e-5 landing site. Local surface at the landing site is a relatively flat mare plain, while superposed by many small, sub-kilometer impact craters.

Slope-imaging map, calculated from the Kaguya TC DTM topography in a moving 3 × 3-pixel kernel with a baseline of 30 m, demonstrates that the local mare plain near the landing site is very flat at the decameter scale, with ~88% of surface having topographic slope less than 5° (Figs. 4c, d). Topographic slope at the Chang'e-5 landing site is measured less than 2°, an excellent topographic condition for controlled soft landing and surface sampling operations. Local steeper slopes primarily occur at the flank of the Louville ω kipuka and at the inner walls of many relatively larger (> ~ 100–200 m) and fresh impact craters (Fig. 4c). The mare ridges, including the small one in the west nearby of

the landing site and the large ones at the northwestern and southwestern corners, while distinctly present on low-sun imaging and altimetric maps (Fig. 3), are not perceptible on the slope image. We ascribe this observation disparity to the contrast between the slope map baseline (30 m) and the dimension of these ridge features (kilometer-scale): the topographical relief of these ridges mainly manifest at kilometer scale, while many parts of these ridges (e.g., the broad gentle arch) can be relatively flat at decameter scale (comparable with typical mare plain surface).

4.2. Impact craters and secondaries of the landing area

We next survey the geomorphology of the 20 × 20 km landing area using low-sun (10–20° solar elevation angle) LROC NAC images. Other than the mare ridges and Louville ω investigated above, the landing area is less complicated in surface morphology. The primary landscape across the landing area is relatively flat lava plain, superposed by many sub-kilometer impact craters (Fig. S3). Pristine lava flow features, like flow lobes and lava flow fronts seen at many terrestrial volcanic fields, are not observed across the landing area, indicating that the mare deposits at the Chang'e-5 landing site are primarily cooling-limited lava flows commonly ~10 m thick, whose initially-formed topographical relief and marginal features have been progressively smoothed out by impact-induced topographical erosion process (Soderblom, 1970), a common eruption and evolution sequence for mare effusive eruptions on the Moon (Head and Wilson, 2017).

The prevalent morphological features across the landing area are abundant circular craters with a wide range of sizes, likely primary impact craters. All the impact craters in the landing area are less than 1 km in diameter. The largest crater occurs at 5.7 km northwest of the landing site (Figs. S3 and 5a), with a diameter ~ 780 m and a rim-to-floor depth of ~105 m (measured from Kaguya TC DTM topography). A depth/diameter ratio of ~0.13, relatively steep and blocky interior walls, while more degraded crater rims designated it a relatively fresh B-class crater (Basilevsky, 1976). Extremely fresh craters are also identified at many locations in the landing area, like the one mapped in Fig. 5b, with a measured diameter of 310 m. Extensive fields of boulders up to over 10 m in size occur within and on the exterior ejecta of this crater, proposing it as a A-class crater (Basilevsky, 1976) and the most immature materials in the landing area. This fresh crater is comparable in size with, but blockier than the 340-m diameter, 25-Ma old Cone crater near the Apollo 14 landing site (Stöffler and Ryder, 2001), suggesting that the former crater is younger than 25 Ma. In addition to these typical bowl-shaped craters, many craters have developed peculiar interior structures, including concentric (Fig. 5c) and central-mounded patterns (Fig. 5d). These special interior structures are interpreted as impacts into layered targets (typically an unconsolidated regolith layer overlain on a more cohesive basaltic substrate; Quaide and Oberbeck, 1968). Diameter measurements of these craters and their interior structures estimate the regolith thickness as ~5 m, generally consistent with prior investigations (Yue et al., 2019; Qian et al., 2021a).

The nearby vicinity (1 × 1 km) of the Chang'e-5 landing site (Fig. 6a) is dotted with abundant impact craters. This is visually testified by the sequences of images taken by the Chang'e-5 LCAM during the soft-landing procedure (e.g., Fig. 6c; a video compilation can be found at http://moon.bao.ac.cn/mul/media/detail?id=554). These craters are characterized by a wide range of degradation status, from very fresh ones with blocky interior wall and exterior ejecta, to highly degraded ones nearly impossible to recognize. A ~ 400-m-diameter crater lies ~200 m northwest of the landing site (informally designated as "NW-400 crater", Fig. 6a). This crater has comparable morphological crispness and crater wall blockiness with the aforesaid 780-m B-class crater (Fig. 5a). The Chang'e-5 landing site very likely lies on the continuous ejecta blanket of this crater; this observation has very important implications for Chang'e-5 sample analyses (Section 5). The landing site is surrounded by three prominent sub-decameter craters at distances of

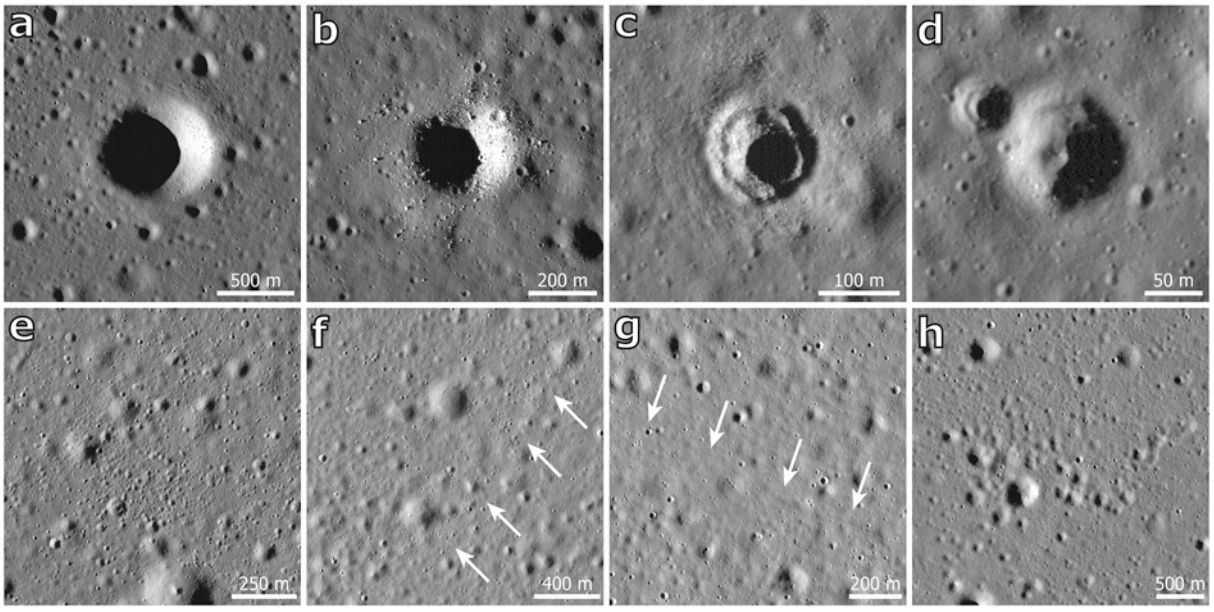


Fig. 5. Primary and secondary impact cratering landforms in the Chang'e-5 landing area: (a) regionally largest (~780 m in diameter) crater ~6 km northwest of the landing site, LROC NAC frame M102500332R, 1.62 m/pixel, 78.8° incidence angle (*i*), (b) one of the regional freshest and blockiest craters, ~310 m in diameter, ~5.5 km west of the landing site, with abundant boulder fields within this crater and on the ejecta, NAC frame M102500332R, (c) a concentric crater at the northern margin of the studied landing area, ~140 m in diameter, NAC frame M1200452194L, 1.29 m/pixel, $i = 77.1°$, (d) a central-mounded crater near to the northern margin of the studied landing area, ~115 m in diameter, NAC frame M1200452194L, (e) a cluster of abundant small craters ~9 km northeast of the landing site, NAC frame M1185180055R, 1.40 m/pixel, $i = 76.9°$, (f) a chain of small craters (white arrows) aligned in a northeast-southwest direction, ~4 km south of the landing site, NAC frame M1200452194L, (g) a set of linear parallel furrowed textures (pointed out by the white arrows) arranged in a northwest-southeast direction in the western edge of the landing area, NAC frame M102500332L, 1.63 m/pixel, $i = 78.6°$, and (h) secondary crater clusters ~1 km north of the landing site, NAC frame M1173414625R. The locations of these NAC images are shown as white boxes in Fig. S3.

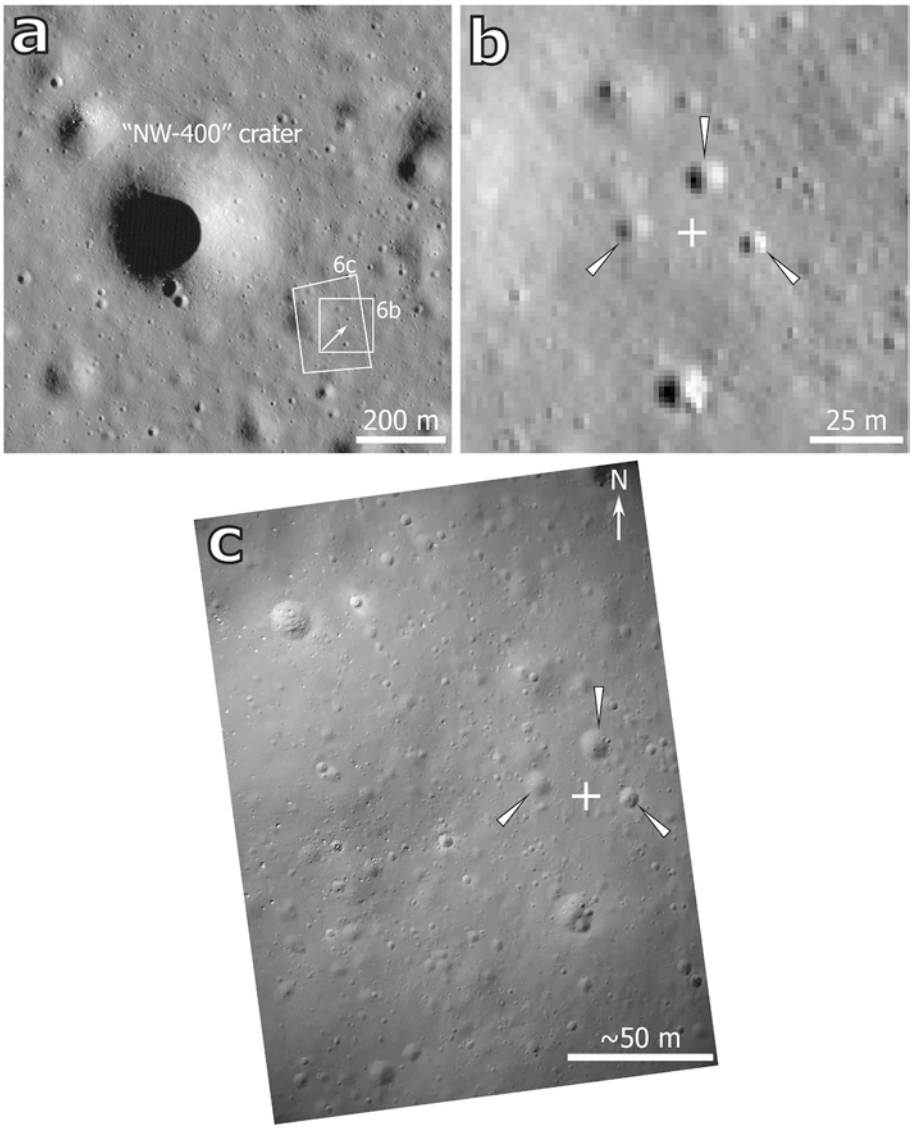


Fig. 6. The very nearby vicinity of the Chang'e-5 landing site (marked by white arrow in panel a and white crosses in panels b and c). (a) A 1 × 1 km area surrounding the landing site, LROC NAC frame M1173414625R, 1.41 m/pixel, i = 75.4°. The location of this NAC image is shown in Fig. S3, and the extents of panels b and c are marked with the white square and polygon, respectively. (b) The nearby 120 × 120 m area surrounding the landing site, NAC frame M1173414625R. The three sub-decameter craters around the landing site are pointed out by the elongated triangles (also in panel c). (c) Ultra-high-resolution image of the landing area taken by the LCAM aboard the Chang'e-5 lander, LCAM frame 349 (credit: Data Release and Information Service System of China's Lunar Exploration Program).

~10 m: a ~ 10-m crater in the north, a ~ 8-m one in the west and a ~ 7-m one in the east (pointed out by elongated triangles in Figs. 6b, c). Ultra-high-resolution centimeter-scale LCAM images taken at a very low altitude revealed many tiny craters and boulders that are otherwise unresolved in orbital LROC NAC images (Fig. 6c).

In addition to typical circular simple craters, another set of prominent landforms in the landing area is surface features and textures related to secondary impact cratering by ejecta from larger primary craters. Secondary cratering features near the landing site are characterized by a variety of morphologies and spatial distribution patterns (Figs. 5e-f). Some occur as concentrations of numerous small craters with an unusually high areal density (Fig. 5e). Chains of abundant small craters are also common appearances of secondaries on flat maria (Fig. 5f); their characteristic spatial distribution patterns provide an insight to track their primary source crater locations. A set of linear parallel furrowed textures is observed at the northwest and northeast marginal portions of the studied landing area (Fig. 5g). These linear features are generally 1–2 km long, up to ~30 m wide and dominantly develop in the northwest-southeast direction. They exhibit distinctive surface textures, while are very subtle in topographical relief and almost unresolved in Kaguya TC topography (Fig. 4). Similar furrowed lineaments were also seen near the Chang'e-4 landing area (Qiao et al., 2019) and associated with some lunar impact basins (e.g., Head, 1976b), which were interpreted as erosional landforms sculpted by crater ejecta.

A prominent cluster of secondary craters occurs ~1 km north of the Chang'e-5 landing site, spanning an area of ~3 × 2 km (Fig. 5h). This secondary crater cluster is well-preserved, with distinct crater rims. Individual craters are characterized with elliptical or "herringbone" shapes, with lengths up to ~300 m. Abundant secondary cratering features suggest that a considerable amount of material from distant craters has been deposited at the Chang'e-5 site and has been potentially sampled and returned to the Earth. These ejecta materials may provide crucially important chances for the on-going Chang'e-5 sample analyses, like the putative samples ejected from Copernicus and Tycho craters in the Apollo 12 and 17 sample collections, the isotopic ages of which contributed two vital calibration points to the lunar chronology function (Stöffler and Ryder, 2001). We will address this issue further in the discussion section (Section 5).

4.3. Chemical composition of the landing area

Elemental concentration mapping results from Kaguya MI multispectral images (20 m/pixel) reveal that the local surface surrounding the Chang'e-5 landing site is relatively homogeneous in surface iron and titanium abundances (Fig. 7), which resonates with the observed relatively monotonous surface morphology across the landing area (section

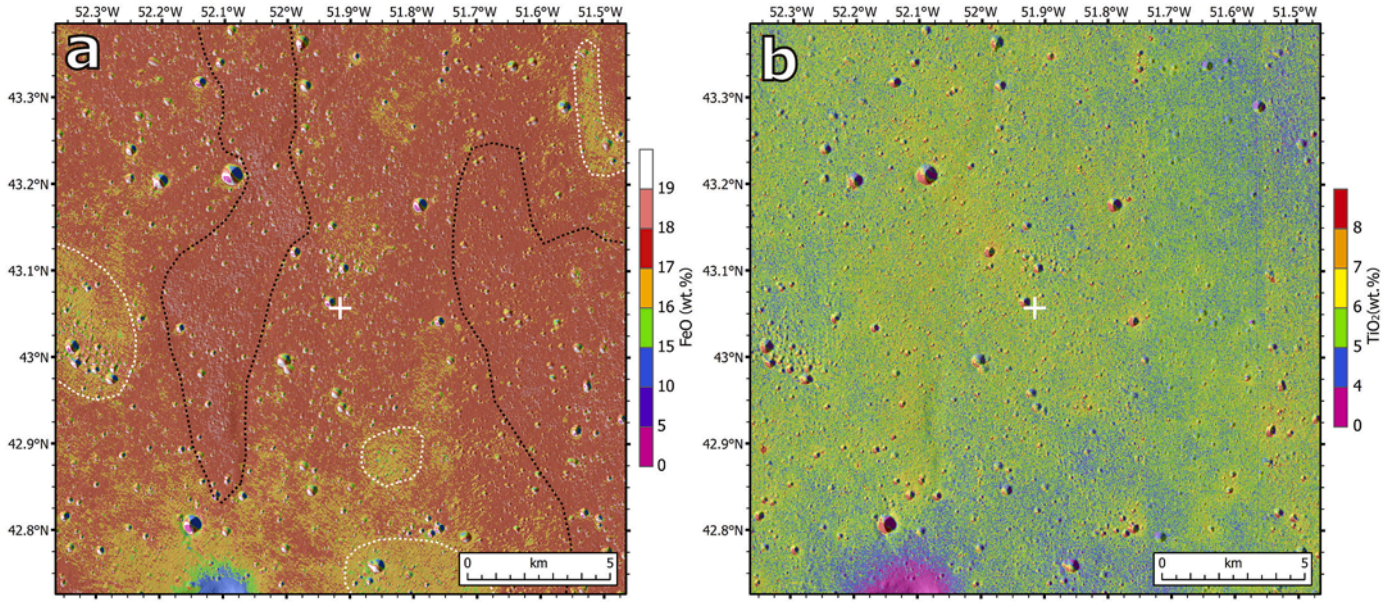


Fig. 7. (a) FeO and (b) TiO_2 content maps of the 20 × 20 km area surrounding the Chang'e-5 landing site (marked by the white crosses, overlain on Kaguya TC morning image mosaic), derived from Kaguya MI reflectance images using algorithms of Lemelin et al. (2015) and Otake et al. (2012), respectively. The white and black dotted polygons in panel a delineate the areas heavily contaminated by and largely free of foreign ejecta materials with reduced iron contents, respectively.

4.2). The majority (92–96%) of the landing area has an inferred surface FeO content between 16 and 19 wt% and TiO_2 content between 4 and 7 wt% (Figs. 7 and S4). The 20 × 20 km landing area has an average FeO content of 17.3 wt% and TiO_2 content of 5.6 wt%. The spatial distribution of iron and titanium abundance maps overlap each other, suggesting ilmenite ($FeTiO_3$) as the major carrier of titanium. A ~ 6 wt% average TiO_2 content would infer an ilmenite mineral abundance of ~11 wt%, showing that mare basalts at the Chang'e-5 sampling site are more titanium-rich than most (~90%) of the mare surface on the global Moon (Giguere et al., 2000). Spatial deconvolution processing of the Lunar Prospector gamma ray spectrometer (GRS) datasets constrains the surface thorium (Th) abundance (with a footprint size of ~45 km, Fig. S5; Lawrence et al., 2002) at the Chang'e-5 landing area to 6.3 ppm (parts per million), a typical enrichment of thorium element for the unique Procellarum KREEP Terrane (PKT).

Integrating high-resolution geochemical mapping results and morphological interpretations from optical surface images (section 4.2) identifies many compositional anomalies and variations across the landing area (Fig. 7). (1) Most of the extreme compositional values (FeO < ~15 or > ~19 wt%, TiO_2 < ~4 or > ~8 wt%) occur at crater interior walls, and sharp changes in composition are observed between the northern and southern portions of crater walls (Fig. 7), revealing that compositional mapping results at these topographically complex areas are unreliable, largely due to improper calibration of the MI reflectance data. Additional element content maps from Clementine UVVIS (Lucey et al., 2000) and Chandrayaan-1 M^3 (Bhatt et al., 2019) may help reduce the composition estimation errors. (2) Another major compositional anomaly is the Louville ω kipuka at the southern edge of the 20 × 20 km landing area (Fig. 7). Its apparently lower iron (FeO <15 wt%) and titanium (TiO_2 < 4 wt%) contents compared with the adjacent mare basalts confirm its non-mare nature, not a volcanic mare kipuka that was formed by partial flooding of pre-existing mare deposits (Head, 1976a). (3) Obvious compositional variations are not observed to be associated with ejecta deposits surrounding the impact craters across the landing area (Fig. 7), even for the largest crater (up to ~780 m in diameter, section 4.2 and Fig. 5a), indicating that these craters are not large enough to penetrate the surficial basaltic deposit layer, and excavate underlying pre-emplaced mare materials (inferred as older Imbrian-aged low-titanium basalts). This reveals that the P58 mare unit at the landing site is thicker than the maximum excavation depths of these superposed craters (0.084 × crater rim-to-rim diameter = 65 m; Melosh, 1989). Our thickness estimation (>65 m) is consistent with recent investigation results by Qian et al. (2021a; ~77 m thickness low limit for their subunit 14). (4) In addition, examination of the MI compositional maps, especially the iron content map, identifies several areas with lower iron and titanium contents (~16–17 wt% FeO, delineated with the white dotted polygons in Fig. 7a). Their spatial distribution patterns and the observation of abundant superposed small crater clusters and chains (section 4.2 and Fig. 5) indicate that these areas have been contaminated by low-iron materials. We also select two areas largely free of contamination of foreign ejecta to represent the local pristine mare basalts (black dotted polygons in Fig. 7a) and determine their average composition of 17.6 wt% FeO and 5.8 wt% TiO_2. The Chang'e-5 landing site seems to be located in a local field of abundant northwest-southeast-trending lineaments with lower iron contents (Figs. 7a and S6), suggesting that surface materials at the Chang's-5 sampling site may contain considerable amount of distant ejecta components. This would potentially contribute to the diversity of Chang'e-5 returned samples, while also complicate sample analyses and interpretations (Section 5).

4.4. Mineral composition of the landing area

We investigate the mineralogical composition of the mare units surrounding the Chang'e-5 landing site using M^3 orbital hyperspectral imaging data. M^3 color composite image mosaic (IBD1000 in the red channel, IBD2000 in the green and reflectance at 1.58 μm in the blue; Fig. 8a) shows that the multiple mare units surrounding the landing site (P58, P10, and P3) are generally reddish or yellowish-green in color, in contrast to the bluish non-mare units. A yellowish-green color in the M^3 color composite map reveals spectral absorptions at both 1 and 2 μm, suggesting mineral pyroxene as the dominant mafic component. To verify this interpretation, we pick dozens of fresh sub-kilometer craters superposed on these mare units to represent the unweathered pristine basaltic materials of their host mare units (points in Fig. 8a). We collect M^3 reflectance spectra from these small craters (Fig. 8b) and remove the continuum (Fig. 8c), all of which show diagnostic 1 μm and 2 μm absorption features of pyroxene. The continuum-removed spectra are also polynomially fitted to determinate the absorption band center

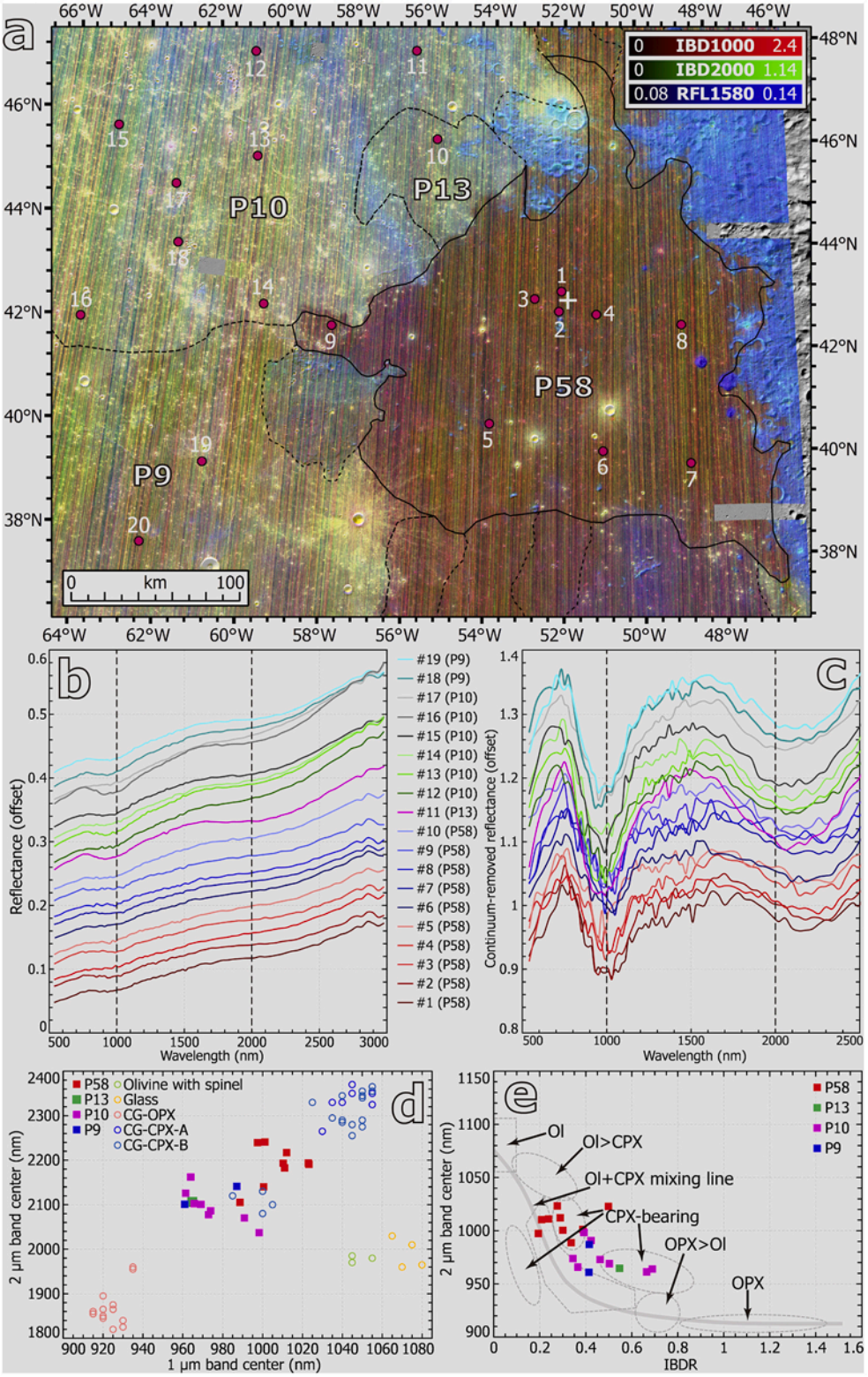


Fig. 8. M^3 spectroscopic investigations of mare units surrounding the Chang'e-5 landing site: (a) color composite image mosaic (red is IBD1000, green is IBD2000 and blue is reflectance at 1.58 μm), the Chang'e-5 landing site is marked by the white cross and small fresh craters for spectral analyses are marked by magenta points; (b) raw and (c) continuum-removed spectra of small mare craters, all spectra are offset by 0.02 incrementally for clarification; (d) plot of 1 and 2 μm absorption center wavelengths of small mare craters, in the context of pyroxene data from Horgan et al. (2014); (e) plot of IBDR against 1 μm band center (Gaffey et al., 2002). In panel a, the boundary of the P58 mare unit surrounding the landing site is indicated by the bold black polygon and the other mare units are delineated by the dashed black polygons. (For interpretation of the references to color in this figure legend, the reader is referred to the web version of this article.)

wavelength. Band centers at 1 μm are plotted against 2 μm band centers, in the background of a suite of pyroxene with range of compositions (Horgan et al., 2014), to investigate the composition of pyroxene (relative Ca, Mg, and Fe abundances) in these mare units (Fig. 8d). The absorption centers of these small craters are generally in the trendline of pyroxene and close to clinopyroxene. This shows that the pyroxenes in these mare basalts are relatively calcium-rich, consistent with mineral abundance mapping results of Qian et al. (2021a) from Kaguya MI global mineral abundance data sets (Lemelin et al., 2015 and remapped in Figs. S7–10). Small craters in the P58 mare unit at the landing site have longer 1 μm and 2 μm band center wavelengths, suggesting that mare basalts near the landing sites contains more clinopyroxene components than the western mare units or the pyroxenes in the P58 unit are more Fe-rich than those in western maria (Fig. S9).

In addition, the M^3 color composite map also shows that the P58 mare unit at the landing site is relatively redder in hue than the older mare units in the west (P13, P10, and P9). This observation reveals that mare deposits at the landing site have relatively stronger absorption at 1 μm (compared to 2 μm band) than those of the western mare units, suggesting the enrichment of clinopyroxene and olivine for the P58 mare basalts. To further confirm the nature of the redder P58 unit, we calculate the ratios between the IBD at 1 μm and 2 μm (IBDR), and plot them against the 1 μm absorption band centers (Fig. 8e). Data points from P58 mare units are located in the spectral fields defined by olivine-clinopyroxene mixing fields (Gaffey et al., 2002), and closer to olivine-rich mineral assemblages ("Ol" and "Ol > CPX" areas in Fig. 8e) than those of the western mare units (P13, P10, and P9, closer to OPX-rich fields). We suggest that the P58 mare unit at the landing site appears to be more clinopyroxene- and olivine-rich than other adjacent mare units, consistent with M^3 spectroscopic investigation of the late-stage volcanic basalts in the western lunar nearside (Staid et al., 2011), which showed that the P58 mare unit was among the most olivine-rich basalts on the Moon.

We address that the olivine abundance mapping results for the maria surrounding the Chang'e-5 landing site from radiative transfer modeling of Kaguya MI data (Lemelin et al., 2015 and referred by Qian et al., 2021a) is probably of significant uncertainty on the basis of at least the following two observations (Fig. S7). (1) The olivine abundance of the P58 mare unit seems to be lower than that of the western mare units (P10), which is inconsistent with M^3 color composite maps (Staid et al., 2011 and Fig. 8a). This is probably attributed to the high ilmenite abundance in the P58 mare basalts (estimated as ~11 wt%), which is an opaque mineral and causes significant surface darkening, but not considered in the modeling of Kaguya MI mineral maps. In addition, the MI maps also suffer from apparent stripe noises (Fig. S7–10), which make the mineral mapping results surrounding the Chang'e-5 landing area probably unreliable. (2) Many locations with abundant secondary crater clusters and chains (pointed out by the elongated triangles in Fig. S7) are characterized by anomalously elevated olivine abundance. This is probably unreliable, as many of these secondary fields are contaminated by iron-depleted highland materials, which is testified by iron content mapping results (our Fig. 7 and Fig. 9 of Qian et al., 2018). Average mineral abundant values calculated from a comparatively larger region may give more meaningful results as many map pixels can be artifacts. Whereas, these observed olivine variations between different mare units are close to the alleged $1\sigma = 8$ wt% uncertainty of the MI mineral abundance data sets (Lemelin et al., 2015). This implies the significant uncertainty for quantitative compositional analysis results from remote sensing measurements. Laboratory high-accuracy compositional measurements of returned Chang'e-5 sample will clarify these uncertainties and help calibrate and ground-truth remote sensing data sets.

5. Discussion and implications for Chang'e-5 sample analyses and interpretations

5.1. Geochemical and chronological characteristics of mare basalts at the Chang'e-5 sampling site

Analyses of returned lunar basalt samples quickly identified their strikingly large variation of titanium contents, ranging from less than 1 wt% to ~14 wt% of TiO_2 (Taylor et al., 1969; Papike et al., 1976). This titanium content range is too large to be generated through fractional crystallization, and is thus attributed to chemical composition differences of the magma sources (Papike et al., 1976). Lunar mare basalts are consequently categorized per their titanium contents for further petrological analyses. In addition, synthesis of sample data also suggested a bimodal titanium distribution of mare basalt, with a distinct compositional gap (~5–9 wt% TiO_2) between high-titanium (>9 wt%) and low-titanium (<5 wt%) basalt suites (Papike et al., 1976; Neal and Taylor, 1992; Fig. 9a), though a few intermediate-titanium basalts have also been recognized in the Apollo sample collections, for instances, clasts extracted from Apollo 14 breccia 14063 (Neal and Taylor, 1992). Whereas, remotely-sensed spectral data suggested a continuous distribution of titanium abundances for lunar global mare basalts, and the intermediate-titanium basalts were largely not sampled by the Apollo/Luna missions (Pieters, 1978; Lucey et al., 1998).

A FeO-TiO_2 content plot clearly discriminates mare basalts at the Chang'e-5 sampling site from all typical classes of lunar basalts collected by Apollo and Luna missions (Fig. 9a). Mare basalts at the Chang'e-5 site have comparable iron content with some of Apollo 11 low-potassium and feldspathic (Apollo 12 and 14 and Luna 16) basalts, while they have intermediate titanium content and occupy the ~5–9 wt% TiO_2 compositional gap in the Apollo/Luna mare basalt sample collections. The samples returned by the Chang'e-5 mission likely represent a new type of lunar mare basalt. Laboratory high-accuracy chemical analyses of these samples will potentially provide new "ground truth" for calibrating compositional mapping of global lunar surface from remote sensing spectral data sets. These new samples also provide an extraordinary opportunity to investigate the thermal history of the Moon and the nature of lunar interior that were probably not fully represented by the Apollo and Luna samples.

We also compare the titanium contents and ages of mare basalts at the Chang'e-5 sampling site with those of nearly 500 mare units elsewhere on the Moon (Fig. 9b), as mare basalts were previously proposed to exhibit a correlation between titanium abundance and age (e.g., Papike et al., 1976; Head, 1976a; Morota et al., 2011). It shows that the P58 mare unit at the Chang'e-5 site has comparable titanium content with other young mare units in Oceanus Procellarum. In addition, the P58 mare unit also lies on the composition-age trend of Oceanus Procellarum basalts with younger basalts tending to be relatively titanium-rich (Fig. 9b), as suggested in prior work (Morota et al., 2011; Sato et al., 2017). This characteristic correlation between titanium content and age may reflect compositional evolution of magma source of lunar late-stage volcanism or vertical compositional heterogeneity of the lunar upper mantle. Analyses of Chang'e-5 samples will provide key evidence for constraining the nature of geological and thermal evolution of the last ~1–2 Ga of lunar history.

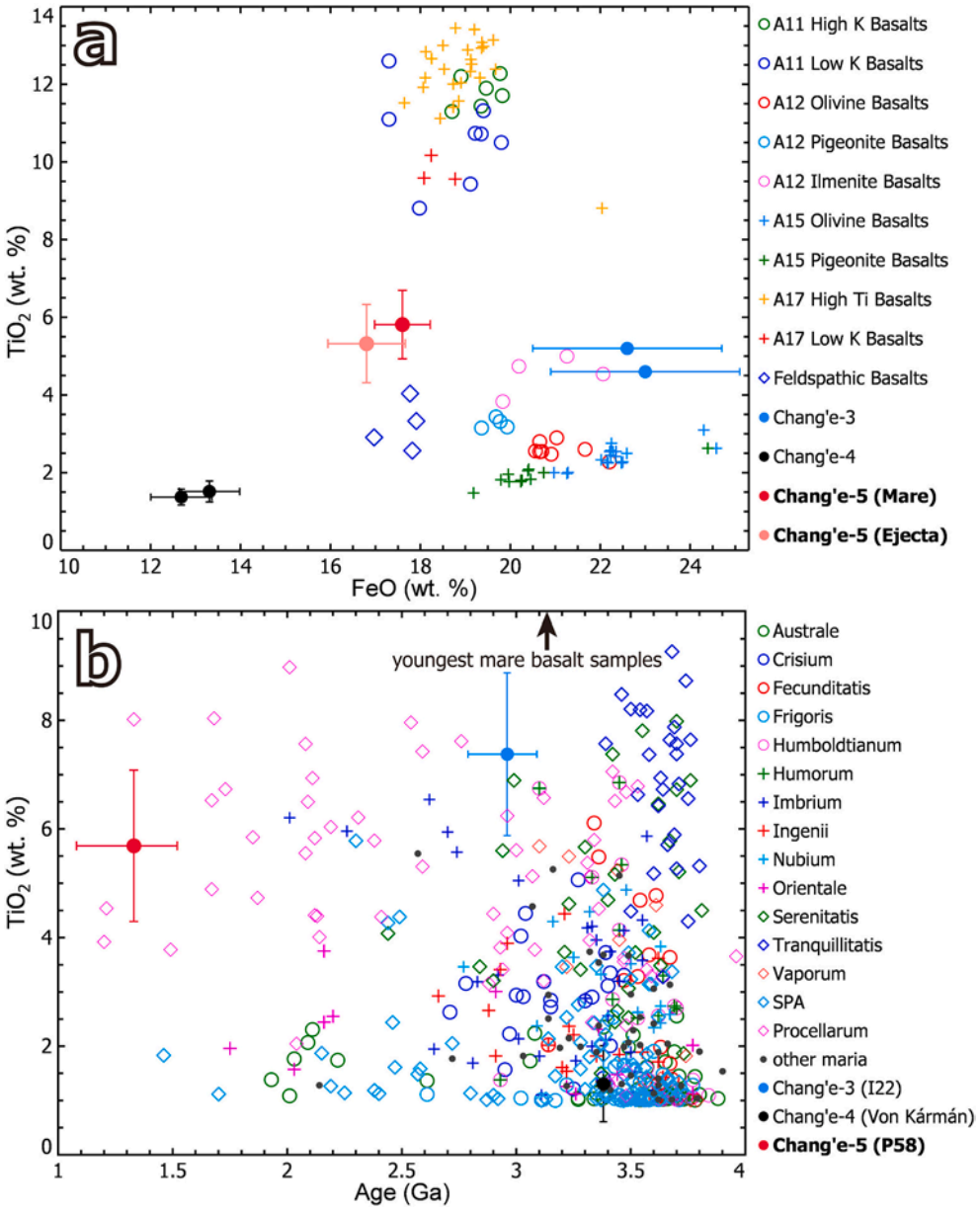


Fig. 9. (a) Comparison of FeO and TiO_2 abundance of mare basalts at the Chang'e-5 sampling site (the area delineated by black dashed polygons in Fig. 7a; the error bars represent 1σ errors) with all typical types of lunar mare basalt samples collected by Apollo and Luna missions (Papike et al., 1976), mare basalts in Chang'e-4 landing area in Von Kármán crater (Qiao et al., 2019) and Chang'e-3 surface in-situ geochemical measurements (Ling et al., 2015). The mare area contaminated by low-iron materials (white dashed polygons in Fig. 7a) is also plotted here. (b) TiO_2 abundance (calculated from Kaguya MI data using the Otake et al. (2012) algorithm) as a function of crater counting model ages for 482 mare units (compiled from previous mare dating work: Cho et al., 2012; Haruyama et al., 2009; Hiesinger et al., 2006, 2011a, 2011b; Ling et al., 2019; Morota et al., 2009, 2011; Pasckert et al., 2015, 2018; Tyrie, 1988; Whitten et al., 2011). Mare units at Chang'e-3/4/5 (I22/Von Kármán/P58) are highlighted by larger markers and the error bars are 1σ errors.

5.2. *Geological events potentially recorded in Chang'e-5 samples: ages and sources of material*

On the basis of our detailed geological characterization of context area of the Chang'e-5 sampling site at various scales, we identify the following geological events that are potentially recorded in the returned samples, in a chronological sequence:

5.2.1. *The Eratosthenian-aged mare volcanism that emplaced the P58 mare unit*

Rima Sharp, the longest sinuous rille discovered on the Moon, which lies ~17 km east of the sampling site, is the likely source of the mare materials collected by the Chang'e-5 mission. Petrological analyses of Chang'e-5 mare basalt samples will provide key information for assessing the eruption environments of lunar sinuous rille-formation volcanism, including magma source depth, magma properties (especially volatile contents) and effusion flux. The P58 mare unit has been dated to be 1.33 Ga old through crater population analyses (Hiesinger et al., 2003), though the dating result has been updated subsequently as ~1.2–2.2 Ga (Table S1). Despite the large variations of dating results for the same mare unit, the mare basalt samples collected by Chang'e-5 are plausibly among the youngest mare units identified from remote sensing data on the Moon and much younger than any lunar basalts collected by Apollo and Luna missions or in meteorites. Detailed laboratory analyses of the Chang'e-5 basalt samples (chemical, mineralogical, petrologic, isotopic, and geochronologic measurements) will provide crucial insights into the late-stage lunar volcanism.

5.2.2. *Post-mare tectonism that formed the western small wrinkle ridge*

The local mare surface surrounding the Chang'e-5 sampling site was subject to post-mare tectonic deformation processes, which resulted in surface uplift and formation of the 20 km long, north-south-oriented wrinkle ridge 2 km west of the Chang'e-5 sampling site. This tectonic activity would have likely modified the micro-structure of specific minerals (e.g., apatite) in the mare basalts. Low-temperature thermochronometric analyses of apatite fission tracks in the Chang'e-5 basalt samples would potentially quantify the formation age and deformation rate of this small mare ridge (Herman et al., 2013; Fox et al., 2014).

5.2.3. The impact that formed the northwestern 400 m crater (NW-400 crater)

After the mare basalt deposition, impact cratering became the dominant geological process that modified the landscape of lunar surface across the Chang'e-5 landing site, and formed numerous impact craters with a wide range of dimensions (section 4.2). One particular crater is the regionally large crater very near to the Chang'e-5 sampling site (Fig. 6a). We employ high-resolution LROC NAC images (1.41 m/pixel) to measure the crater diameter as 394 m and the distance from Chang'e-5 landing site to crater center as only 422 m. On the basis of the empirical model on the spatial extent of ejecta blanket of lunar craters (Melosh, 1989), continuous ejecta is estimated to extend 468 m from the NW-400 crater center. The Chang'e-5 landing site is therefore located on the marginal portion of the ejecta deposits of the NW-400 crater, an important geological context information that have been missed in previous landing area geological investigations.

Measurements from high-resolution TC DTM topography (10 m/pixel) derived a ~ 42 m rim-to-bottom depth for this crater. The calculated depth/diameter ratio of ~0.11, along with the observed relative freshness (e.g., relatively degraded, while still observable rim crest and blocks at crater walls) designate it as a morphologic class-B crater and allow one to estimate its age as ~400 Ma (~338–450 Ma; Basilevsky, 1976). However, we suggest that this age estimation is probably of considerable uncertainty (as had been noted by Basilevsky (1976)) and seems to be in conflict with the observed superposition of rays from the Copernicus crater (~800 Ma old, Stöffler and Ryder, 2001) on its ejecta blanket (see descriptions below). Crater population analysis on the continuous ejecta blanket also fails to get a reliable age for the NW-400 crater due to many challenges, including the very small crater count working area and the difficulty in eliminating craters formed before the NW-400 crater.

From the radial ejecta thickness equation (McGetchin et al., 1973; Pike, 1974), ejecta from the NW-400 crater is predicted to be 0.3–0.4 m thick at the Chang'e-5 landing site. Thus, the returned Chang'e-5 samples may contain a portion of ejecta materials from this NW-400 small crater. While this small crater is not large enough to excavate and eject underlying older mare basalts, it would have exposed long buried subsurface materials (maximum excavation depth ~ 30 m) to the surface and cosmic ray irradiation. Cosmic ray exposure age analyses of the Chang'e-5 samples would potentially constrain the age of this 400-m-diameter crater. In addition, high-velocity impact may cause appreciable degassing of local mare basalts, radiometric-dating analyses of returned samples would potentially identify these degassing events and obtain a reliable age for the NW-400 crater (Stöffler and Ryder, 2001).

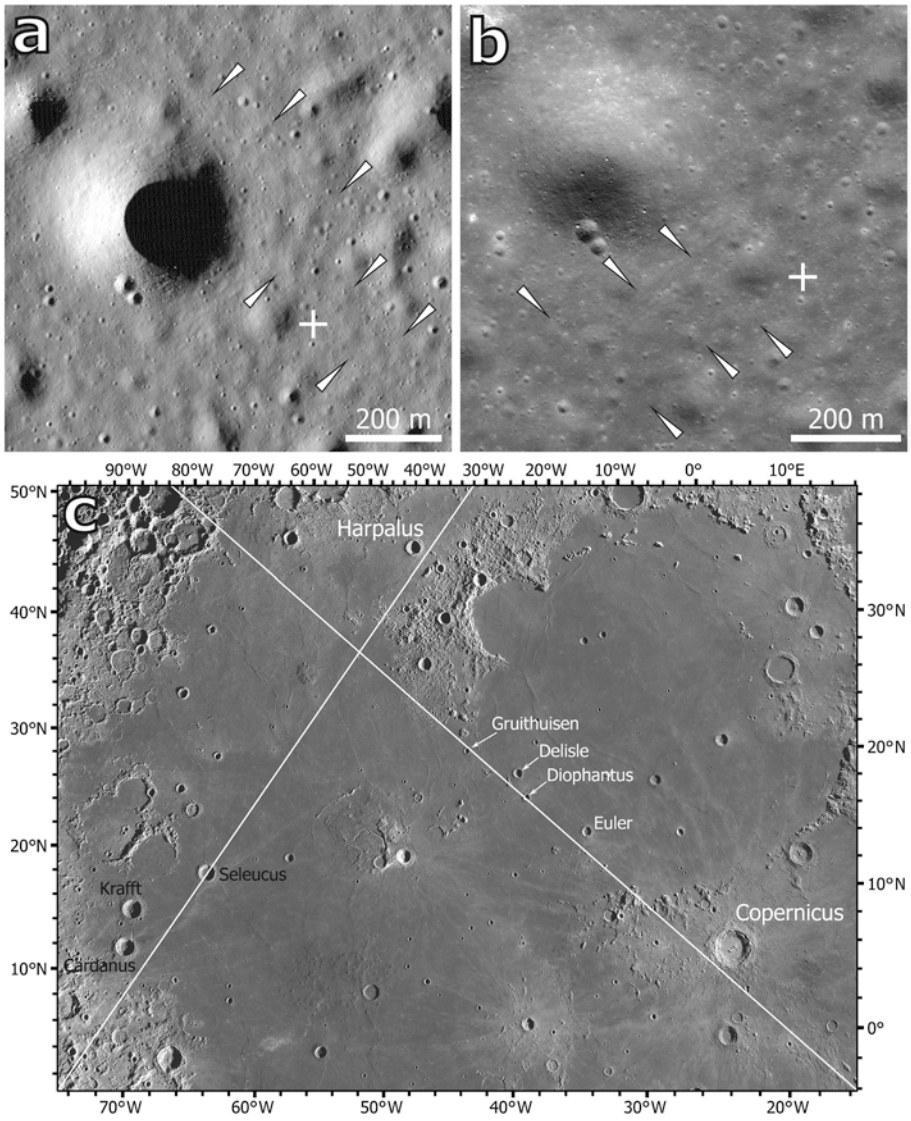


Fig. 10. Ray features crossing the Chang'e-5 landing site and their inferred source craters. (a) A set of northwest-southeast-trending rays at the landing site, LROC NAC frame M1200452194L. (b) Another set of northeast-southwest-trending rays, NAC frame M1132169436L, 1.1 m/pixel, $i = 45.6°$. (c) Great circles extended from the trends of the ray features in panels a and b, LROC WAC low-sun mosaic. In (a) and (b), the Chang'e-5 landing site is marked by the white crosses, and the ray patterns are pointed out by elongated triangles. In (c), potential large craters along the trend line are identified by their names in white. The three craters along the trend line, while stratigraphically older than the Chang'e-5 landing site mare unit, are labelled with their names in black.

5.2.4. Copernican-aged large impacts that delivered ray materials to the Chang'e-5 sampling site

Secondary cratering features with a range of morphologies have been identified across the Chang'e-5 landing area (section 4.2). Such features are also directly observed to cover the Chang'e-5 sampling site. A prominent set of linear parallel shallow furrowed textures, ranged in a northwest-southeast direction, appears to cross the Chang'e-5 site (Fig. 10a). Though these lineaments are not deep enough to be measurable in topography data, their albedo variations and morphological characteristics are apparently seen in meter-scale LROC NAC images. Their distinctive spatial distribution patterns can be used to assess their source regions. Due to their subtle topographical and morphological signatures, it is difficult to determinate which is the uprange direction. So, we map out the direction of these lineaments and extend it in both southeast and northwest directions on a WAC map in a Lambert conformal conic projection centered at the Chang'e-5 landing site (Fig. 10c). We find that Copernicus crater and four other smaller craters (Gruithuisen, Delisle, Diophantus, and Euler) are both near to the trends of these lineaments and possibly younger (Eratosthenian or Copernican) than the P58 mare unit (~1–2 Ga). These craters are all located in the southeast direction of the landing site. Among them, Copernicus is the largest (96 km in diameter compared with 15–26 km of other craters) and youngest (Copernican-aged compared with Eratosthenian-aged; Wilhelms and McCauley, 1971; Fortezzo et al., 2020). Ejecta thickness calculation also shows that the predicted ejecta from the Copernicus crater is more than one order of magnitude thicker than those from the other four smaller craters (~3 cm compared with ~0.1–0.3 cm; Pike, 1974). Therefore, we suggest that the Copernicus crater is very likely the source of southeast-trending ray materials at the Chang'e-5 sampling site.

In addition, we also identify another set of northeast-trending ray feature crossing the Chang'e-5 landing site (Fig. 10b). Along the trend of these ray patterns, we find the Copernican-aged (Wilhelms and McCauley, 1971) 40 km-diameter crater Harpalus, located 340 km northeast of the landing site, to be the most likely source of these northwest-trending rays. Three other large craters in the southwest direction (Seleucus, Krafft, and Cardanus) are also near to the trend line (Fig. 10b), although they are all Imbrian-aged (Wilhelms and McCauley, 1971) and much older than the mare flows at the landing site. Ejecta from Harpalus is estimated to be ~9 cm at the Chang'e-5 landing site (Pike, 1974). Some of previous landing area analyses have calculated the thickness of hypothetical ejecta materials from Copernicus and Harpalus craters using empirical scaling laws, but have not reported direct geological evidences for such foreign components (Xie et al., 2020; Qian et al., 2021b).

Ray materials from Copernicus crater are generally believed to have been sampled by the Apollo 12 mission. From these samples, Copernicus is now widely accepted to be ~800 Ma old (Stöffler and Ryder, 2001 and references therein). The Harpalus crater has been previously mapped as Copernican-aged, though recent crater population study on its continuous ejecta blanket has derived a much older age of 2.4 Ga (Xie et al., 2020; this work also found that their crater counting ages are generally older than stratigraphic ages for most of their studied craters ($n = 15$)). These two sets of ray features are also observed to superpose on the rim ejecta of the NW-400 crater (Figs. 10a, b), illustrating clearly that the NW-400 crater is older than Copernicus, and the age estimation from crater morphology classification (~400 Ma; Basilevsky, 1976) is probably unreliable.

Returning potential ray samples from the Copernicus crater for the second time 51 years after the Apollo 12 mission is scientifically very interesting. The generally well known ~800 Ma age of Copernicus crater can be used to assist in interpreting the chronological analysis results of Chang'e-5 samples. Moreover, identification, age dating and detailed characterization of possible ray materials in the Chang'e-5 new samples would also strengthen our understanding on the ages and nature of the Harpalus and Copernicus craters, a critically important parameter for stratigraphy system of the Moon.

In summary, we have identified multiple geological events (volcanism, tectonism, and impact cratering) that are potentially recorded in the returned Chang'e-5 samples. These events are characterized with clear stratigraphic sequences and have taken place within approximately the last 1 Ga of lunar history. More importantly, most of these ages lie in the age gap (~0.8–3.1 Ga) of the current Apollo and Lunar samples, the basis for lunar cratering chronology function commonly used for crater population dating analyses in unsampled lunar surface (Stöffler and Ryder, 2001). Precise ages of these geological events from Chang'e-5 sample analyses would provide critically important information to narrow down the uncertainties of the lunar cratering chronology function and improve our understanding of the geological history of the entire Moon.

6. Conclusions

On the basis of in-depth geological investigation of the Chang'e-5 landing site presented above, we reach the following conclusions:

(1) Chang'e-5 landed in and returned lunar samples from the northeastern Oceanus Procellarum of the western lunar nearside, site of the last major phase of lunar mare volcanism. The mare unit at the Chang'e-5 landing site is dated as ~1–2 Ga from crater counting studies, much younger than all basalts in the present lunar sample collection and among the youngest basalts on the global Moon. The basalt samples returned by Chang'e-5 will provide an unprecedented opportunity to characterize the late-stage lunar volcanism.

(2) Regionally, the Chang'e-5 landing site is <20 km west of Rima Sharp, the longest (over 500 km) sinuous rille catalogued on the Moon. High effusion-rate and long-lived mare eruptions that formed the Rima Sharp may also source the mare basalts collected by the Chang'e-5. A 20-km-long and ~ 20-m-high mare ridge occurs just 2 km west of the landing site. Laboratorial analyses of the Chang'e-5 samples would potentially shed light on the formation mechanism of sinuous rilles and mare ridges.

(3) Locally, the Chang'e-5 landing site is located on a mare plain characterized by a west-east sloping trend, with an elevation offset of ~60 m across a distance of 20 km. The local 20 × 20 km area surrounding the landing site is topographically very flat at the decameter scale, with nearly 90% of surface having slopes less than 5°, an excellent topographic condition for controlled soft landing and surface sampling operations.

(4) Surface geomorphology across the landing area is relatively monotonous and the primary landforms are abundant sub-kilometer circular impact craters. These craters are characterized with a range of degradation states and interior structures. In particular, the Chang'e-5 landing site is very near to and lies on the continuous ejecta blanket of a ~ 400-m-diameter crater. Chang'e-5 returned samples may contain a portion of ejecta materials from this crater. Isotopically-dating analyses of Chang'e-5 samples would potentially identify this impact event and constrain its formation age.

(5) Secondary impact cratering features, occurring as chains or clusters of small craters and linear parallel furrowed textures, are also commonly seen across the landing area. In particular, two sets of secondary cratering features, one arranged in a northwest-southeast-direction and the other in a northeast-southwest-direction, are identified to cross the Chang'e-5 landing site. The sources of these secondary craters are traced back to Copernicus and Harpalus craters, respectively. The Chang'e-5 mission may have collected materials ejected from these two Copernian-aged craters. This would complicate the samples analyses and scientific interpretations, while also enhance the diversity of the

Chang'e-5 samples. Age dating analyses of the two craters would help revise the stratigraphy system of the Moon.

(6) The mare basalts at the Chang'e-5 landing area have an average composition of 18 wt% FeO and 6 wt% TiO_2, and appear to occupy the titanium content gap of Apollo/Luna samples. The landing site mare unit is characterized by a calcium-rich pyroxene-dominated mineralogy and appears to be more olivine-rich than the western older mare units. The basalt samples returned by the Chang'e-5 likely represent a new type of lunar mare basalts, whose compositional measurements will potentially provide new "ground truths" for calibrating remote sensing data and improve our understanding of lunar thermal history and lunar interior. Secondary crater fields are characterized by lower iron abundances, indicating the landing area has been contaminated by iron-depleted materials.

(7) A sequence of four geological events, including mare volcanism, tectonism, impact cratering, and impact ejecta deposition, are identified to have potentially affected and been recorded in the returned Chang'e-5 samples. Isotopic-dating analyses would obtain accurate ages for these geological events, and reconstruct a detailed regional geological evolution model of the landing area. Furthermore, most of the inferred ages of these geological events lie in the age "gap" of the current Apollo and Luna sample collections. Precise determination of these ages would be invaluable in narrowing down the uncertainties of the lunar cratering chronology function and improve our understanding of the geological history of the entire Moon.

Data availability

All original LRO data and Lunar Prospector thorium map can be found in the NASA Planetary Data System Geosciences Node (https://pds-geosciences.wustl.edu/), the original Chandrayaan-1 Moon Mineralogy Mapper data are available at the NASA Planetary Data System Cartography and Imaging Sciences Node (https://pds-imaging.jpl.nasa.gov/volumes/m3.html), the original Kaguya/SELENE data are archived at SELENE Data Archive (https://darts.isas.jaxa.jp/planet/pdap/selene/), and Chang'e-5 landing camera images are available at Data Release and Information Service System of China's Lunar Exploration Program (http://moon.bao.ac.cn/).

Declaration of Competing Interest

None.

Acknowledgments

We sincerely appreciate the Editor-in-Chief Rosaly Lopes for her very efficient and helpful editorial handling, and Drs. David Blewett and Megha Bhatt for the very constructive comments. L. Q. gratefully acknowledges Dr. Yunhua Wu for the very informative discussions concerning apatite fission track analysis. This work is partly supported by the National Key R&D Program of China (2020YFE0202100), the Pre-research Project on Civil Aerospace Technologies of CNSA (D020204 and D020202), National Natural Science Foundation of China (41703063, 11941001 and 41972322), China Postdoctoral Science Foundation (2020M682164), and the Science and Technology Development Fund of Macau (0079/2018/A2). This is SDU-CPS publication #73.

Appendix A. Supplementary data

Supplementary data to this article can be found online at https://doi.org/10.1016/j.icarus.2021.114480.

References

ACIC (Aeronautical Chart Information Center, United States Air Force), 1967. Rümker. Lunar Chart (LAC) Series LAC-23.

Anand, M., Russell, S., Lin, Y., Wadhwa, M., Marhas, K.K., Tachibana, S., 2020. Editorial to the topical collection: role of sample return in addressing major questions in planetary sciences. Space Sci. Rev. 216, 101. https://doi.org/10.1007/s11214-020-00724-4.

Anderson, J.A., Sides, S.C., Soltesz, D.L., Sucharski, T.L., Becker, K.J., 2004. Modernization of the integrated software for imagers and spectrometers. In: 35th Lunar and Planetary Science Conference. Lunar and Planetary Institute, League City, Texas abstract #2039.

Barker, M.K., Mazarico, E., Neumann, G.A., Zuber, M.T., Haruyama, J., Smith, D.E., 2016. A new lunar digital elevation model from the Lunar Orbiter Laser Altimeter and SELENE Terrain Camera. Icarus. 273, 346–355. https://doi.org/10.1016/j.icarus.2015.07.039.

Basilevsky, A.T., 1976. On the rate of evolution of small lunar craters, seventh lunar science conference. In: Proceedings of 7th Lunar and Planetary Institute, pp. 1020–1055.

Bence, A.E., Holzwarth, W., Papike, J.J., 1972. Petrology of basaltic and monomineralic soil fragments from the sea of fertility. Earth Planet. Sci. Lett. 13, 299–311. https://doi.org/10.1016/0012-821X(72)90105-7.

Bhatt, M., Wöhler, C., Grumpe, A., Hasebe, N., Naito, M., 2019. Global mapping of lunar refractory elements: multivariate regression vs. machine learning. Astron. Astrophys. 627. https://doi.org/10.1051/0004-6361/201935773.

Boardman, J.W., et al., 2011. Measuring moonlight: An overview of the spatial properties, lunar coverage, selenolocation, and related Level 1B products of the Moon Mineralogy Mapper. J. Geophys. Res. Planets 116. https://doi.org/10.1029/2010JE003730.

Borg, L.E., Shearer, C.K., Asmerom, Y., Papike, J.J., 2004. Prolonged KREEP magmatism on the Moon indicated by the youngest dated lunar igneous rock. Nature. 432, 209–211. https://doi.org/10.1038/nature03070.

Boyce, J.M., 1976. Ages of flow units in the lunar nearside maria based on lunar orbiter IV photographs. In: Proceedings of 3rd Lunar and Planetary Science Conference, 3, pp. 2717–2728.

Charette, M.P., McCord, T.B., Pieters, C., Adams, J.B., 1974. Application of remote spectral reflectance measurements to lunar geology classification and determination of titanium content of lunar soils. J. Geophys. Res. 79, 1605–1613. https://doi.org/10.1029/JB079i011p01605.

Cho, Y., Morota, T., Haruyama, J., Yasui, M., Hirata, N., Sugita, S., 2012. Young mare volcanism in the Orientale region contemporary with the Procellarum KREEP Terrane (PKT) volcanism peak period ~2 billion years ago. Geophys. Res. Lett. 39 https://doi.org/10.1029/2012GL051838.

Fortezzo, C.M., Spudis, P.D., Harrel, S.L., 2020. Release of the digital unified global geologic map of the Moon at 1:5,000,000-scale. In: 51st Lunar and Planetary Science Conference. Lunar and Planetary Institute, Houston abstract #2760.

Fox, M., Herman, F., Willett, S.D., May, D.A., 2014. A linear inversion method to infer exhumation rates in space and time from thermochronometric data. Earth Surface Dynamics. 2, 47–65. https://doi.org/10.5194/esurf-2-47-2014.

Gaffey, M.J., Cloutis, E.A., Kelley, M.S., Reed, K.L., 2002. Mineralogy of asteroids. In: Bottke, W.F., Cellino, A., Paolicchi, P., Binzel, R.P. (Eds.), Asteroids III. Univ. of Arizona Press, pp. 183–204.

Giguere, T.A., Taylor, G.J., Hawke, B.R., Lucey, P.G., 2000. The titanium contents of lunar mare basalts. Meteorit. Planet. Sci. 35, 193–200. https://doi.org/10.1111/j.1945-5100.2000.tb01985.x.

Glotch, T.D., et al., 2011. The Mairan domes: silicic volcanic constructs on the Moon. Geophys. Res. Lett. 38, L21204 https://doi.org/10.1029/2011GL049548.

Golombek, M., Plescia, J., Franklin, B., 1991. Faulting and folding in the formation of planetary wrinkle ridges. In: Proceedings of 22nd Lunar and Planetary Science Conference, pp. 679–693.

Haruyama, J., et al., 2008. Global lunar-surface mapping experiment using the lunar imager/spectrometer on SELENE. Earth, Planets and Space. 60, 243–255. https://doi.org/10.1186/BF03352788.

Haruyama, J., et al., 2009. Long-lived volcanism on the lunar farside revealed by SELENE Terrain Camera. Science. 323, 905. https://doi.org/10.1126/science.1163382.

Haruyama, J., et al., 2012. Lunar global digital terrain model dataset produced from SELENE (Kaguya) terrain camera stereo observations. In: 43rd Lunar and Planetary Science Conference. Lunar and Planetary Institute, The Woodlands, Texas abstract #1200.

Head, J.W., 1976a. Lunar volcanism in space and time. Rev. Geophys. 14, 265–300. https://doi.org/10.1029/RG014i002p00265.

Head, J.W., 1976b. Evidence for the sedimentary origin of Imbrium sculpture and lunar basin radial texture. The Moon. 15, 445–462. https://doi.org/10.1007/BF00562252.

Head, J.W., 2020. Chang'e 5 Lunar Sample Return Mission: a Brief Background and Summary, pp. 1–6. http://www.planetary.brown.edu/pdfs/5530.pdf.

Head, J.W., McCord, T.B., 1978. Imbrian-age highland volcanism on the Moon: the Gruithuisen and Mairan domes. Science. 199, 1433–1436. https://doi.org/10.1126/science.199.4336.1433.

Head, J.W., Wilson, L., 2017. Generation, ascent and eruption of magma on the Moon: new insights into source depths, magma supply, intrusions and effusive/explosive eruptions (part 2: predicted emplacement processes and observations). Icarus. 283, 176–223. https://doi.org/10.1016/j.icarus.2016.05.031.

Herman, F., et al., 2013. Worldwide acceleration of mountain erosion under a cooling climate. Nature. 504, 423–426. https://doi.org/10.1038/nature12877.

Hiesinger, H., Head, J.W., Wolf, U., Jaumann, R., Neukum, G., 2003. Ages and stratigraphy of mare basalts in Oceanus Procellarum, Mare Nubium, Mare Cognitum,

and Mare Insularum. J. Geophys. Res. Planets. 108 https://doi.org/10.1029/2002JE001985.
Hiesinger, H., Head III, J.W., Wolf, U., Jaumann, R., Neukum, G., 2006. New ages for basalts in Mare Fecunditatis based on crater size-frequency measurements. In: 37th Lunar and Planetary Science Conference. Lunar and Planetary Institute, Houston, Texas abstract #1151.
Hiesinger, H., Head, J.W., Wolf, U., Jaumann, R., Neukum, G., 2011a. Ages and stratigraphy of lunar mare basalts: a synthesis. Geol. Soc. Am. Spec. Pap. 477, 1–51. https://doi.org/10.1130/2011.2477(01).
Hiesinger, H., van der Bogert, C.H., Reiss, D., Robinson, M.S., 2011b. Crater size-frequency distribution measurements of Mare Crisium. In: 42nd Lunar and Planetary Science Conference. Lunar and Planetary Institute, Houston abstract #2179.
Horgan, B.H.N., Cloutis, E.A., Mann, P., Bell III, J.F., 2014. Near-infrared spectra of ferrous mineral mixtures and methods for their identification in planetary surface spectra. Icarus. 234, 132–154. https://doi.org/10.1016/j.icarus.2014.02.031.
Hurwitz, D.M., Head, J.W., Hiesinger, H., 2013. Lunar sinuous rilles: distribution, characteristics, and implications for their origin. Planet. Space Sci 79-80, 1–38. https://doi.org/10.1016/j.pss.2012.10.019.
Jia, M., Yue, Z., Di, K., Liu, B., Liu, J., Michael, G., 2020. A catalogue of impact craters larger than 200 m and surface age analysis in the Chang'e-5 landing area. Earth Planet. Sci. Lett. 541, 116272. https://doi.org/10.1016/j.epsl.2020.116272.
Lawrence, S.J., Neal, C.R., 2019. Exploring the Moon in the 21st century. Elements. 15, 360–361. https://doi.org/10.1016/10.2138/gselements.15.5.360.
Lawrence, D.J., et al., 2002. Small-area thorium enhancements on the lunar surface. In: 33rd Lunar and Planetary Science Conference. Lunar and Planetary Institute, Houston, Texas abstract #1970.
Lemelin, M., Lucey, P.G., Song, E., Taylor, G.J., 2015. Lunar central peak mineralogy and iron content using the Kaguya Multiband Imager: reassessment of the compositional structure of the lunar crust. J. Geophys. Res. Planets. 120, 869–887. https://doi.org/10.1016/10.1002/2014je004778.
Li, C., Wang, C., Wei, Y., Lin, Y., 2019. China's present and future lunar exploration program. Science. 365, 238. https://doi.org/10.1126/science.aax9908.
Ling, Z., et al., 2015. Correlated compositional and mineralogical investigations at the Chang'e-3 landing site. Nature Communications 6, 8880. https://doi.org/10.1038/ncomms9880.
Ling, Z., et al., 2019. Composition, mineralogy and chronology of mare basalts and non-mare materials in Von Kármán crater: landing site of the Chang'E-4 mission. Planet. Space Sci 179, 104741. https://doi.org/10.1016/j.pss.2019.104741.
Liu, J., et al., 2020. Landing site selection and overview of China's lunar landing missions. Space Sci. Rev. 217, 6. https://doi.org/10.1007/s11214-020-00781-9.
LSPET (Lunar Sample Preliminary Examination Team), 1970. Preliminary examination of lunar samples from Apollo 11. Science. 167, 1325–1339. https://doi.org/10.1126/science.165.3899.1211.
Lucey, P.G., Blewett, D.T., Hawke, B.R., 1998. Mapping the FeO and TiO_2 content of the lunar surface with multispectral imagery. J. Geophys. Res. 103, 3679–3699. https://doi.org/10.1029/97je03019.
Lucey, P.G., Blewett, D.T., Jolliff, B.L., 2000. Lunar iron and titanium abundance algorithms based on final processing of Clementine ultraviolet-visible images. J. Geophys. Res. Planets. 105, 20297–20305. https://doi.org/10.1029/1999JE001117.
McGetchin, T.R., Settle, M., Head, J.W., 1973. Radial thickness variation in impact crater ejecta: implications for lunar basin deposits. Earth Planet. Sci. Lett. 20, 226–236. https://doi.org/10.1016/0012-821X(73)90162-3.
Melosh, H.J., 1989. Impact Cratering: A Geologic Process. Oxford University Press, London.
Meng, Z., et al., 2020. Thermophysical features of the Rümker region in northern Oceanus Procellarum: insights from CE-2 CELMS data. Remote Sens. 12 https://doi.org/10.3390/rs12193272.
Morota, T., et al., 2009. Mare volcanism in the lunar farside Moscoviense region: implication for lateral variation in magma production of the moon. Geophys. Res. Lett. 36 https://doi.org/10.1029/2009GL040472.
Morota, T., et al., 2011. Timing and characteristics of the latest mare eruption on the Moon. Earth Planet. Sci. Lett. 302, 255–266. https://doi.org/10.1016/j.epsl.2010.12.028.
Neal, C.R., Taylor, L.A., 1992. Petrogenesis of mare basalts: a record of lunar volcanism. Geochim. Cosmochim. Acta 56, 2177–2211. https://doi.org/10.1016/0016-7037(92)90184-K.
Otake, H., Ohtake, M., Hirata, N., 2012. Lunar iron and titanium abundance algorithms based on SELENE (Kaguya) multiband imager data. In: 43rd Lunar and Planetary Science Conference. Lunar and Planetary Institute, The Woodlands, Texas abstract #1905.
Papike, J.J., Hodges, F.N., Bence, A.E., Cameron, M., Rhodes, J.M., 1976. Mare basalts: crystal chemistry, mineralogy, and petrology. Rev. Geophys. 14, 475–540. https://doi.org/10.1029/RG014i004p00475.
Pasckert, J.H., Hiesinger, H., van der Bogert, C.H., 2015. Small-scale lunar farside volcanism. Icarus. 257, 336–354. https://doi.org/10.1016/j.icarus.2015.04.040.
Pasckert, J.H., Hiesinger, H., van der Bogert, C.H., 2018. Lunar farside volcanism in and around the south pole–Aitken basin. Icarus. 299, 538–562. https://doi.org/10.1016/j.icarus.2017.07.023.
Pieters, C.M., 1978. Mare basalt types on the front side of the moon: a summary of spectral reflectance data. In: Proceedings of 9th Lunar and Planetary Science Conference, pp. 2825–2849.
Pike, R.J., 1974. Ejecta from large craters on the Moon: comments on the geometric model of McGetchin et al. Earth Planet. Sci. Lett. 23, 265–271. https://doi.org/10.1016/0012-821X(74)90114-9.
Qian, Y.Q., et al., 2018. Geology and scientific significance of the Rümker region in northern Oceanus Procellarum: China's Chang'E-5 landing region. J. Geophys. Res. Planets. 123, 1407–1430. https://doi.org/10.1029/2018JE005595.
Qian, Y., et al., 2020. The regolith properties of the Chang'e-5 landing region and the ground drilling experiments using lunar regolith simulants. Icarus. 337, 113508. https://doi.org/10.1016/j.icarus.2019.113508.
Qian, Y., Xiao, L., Head, J.W., van der Bogert, C.H., Hiesinger, H., Wilson, L., 2021a. Young lunar mare basalts in the Chang'e-5 sample return region, northern Oceanus Procellarum. Earth Planet. Sci. Lett. 555, 116702. https://doi.org/10.1016/j.epsl.2020.116702.
Qian, Y., et al., 2021b. China's Chang'e-5 landing site: geology, stratigraphy, and provenance of materials. Earth Planet. Sci. Lett. 561, 116855. https://doi.org/10.1016/j.epsl.2021.116855.
Qiao, L., Xiao, L., Zhao, J., Huang, Q., Haruyama, J., 2014. Geological features and evolution history of Sinus Iridum, the moon. Planet. Space Sci 101, 37–52. https://doi.org/10.1016/j.pss.2014.06.007.
Qiao, L., Ling, Z., Fu, X., Li, B., 2019. Geological characterization of the Chang'e-4 landing area on the lunar farside. Icarus. 333, 37–51. https://doi.org/10.1016/j.icarus.2019.05.029.
Quaide, W.L., Oberbeck, V.R., 1968. Thickness determinations of the lunar surface layer from lunar impact craters. J. Geophys. Res. 73, 5247–5270. https://doi.org/10.1029/JB073i016p05247.
Robbins, S.J., et al., 2014. The variability of crater identification among expert and community crater analysts. Icarus. 234, 109–131. https://doi.org/10.1016/j.icarus.2014.02.022.
Robinson, M.S., et al., 2010. Lunar reconnaissance orbiter camera (LROC) instrument overview. Space Sci. Rev. 150, 81–124. https://doi.org/10.1007/s11214-010-9634-2.
Sato, H., et al., 2017. Lunar mare TiO_2 abundances estimated from UV/Vis reflectance. Icarus. 296, 216–238. https://doi.org/10.1016/j.icarus.2017.06.013.
Schultz, P., Spudis, P., 1983. Beginning and end of lunar mare volcanism. Nature. 302, 233–236. https://doi.org/10.1038/302233a0.
Schultz, P.H., Greeley, R., Gault, D.E., 1976. Degradation of small lunar surface features. In: Seventh Lunar Science Conference. Lunar and Planetary Institute, Houston abstract #1270.
Sharpton, V.L., 1992. Apollo 17: one giant step toward understanding the tectonic evolution of the moon: geology of the Apollo 17 landing site. In: LPI Technical Report 92–09, Part 1, pp. 50–53.
Smith, D.E., et al., 2010. The Lunar Orbiter Laser Altimeter investigation on the Lunar Reconnaissance Orbiter mission. Space Sci. Rev. 150, 209–241. https://doi.org/10.1007/s11214-009-9512-y.
Snape, J.F., Davids, B., Nemchin, A.A., Whitehouse, M.J., Bellucci, J.J., 2018. Constraining the timing and sources of volcanism at the Apollo 12 landing site using new Pb isotopic compositions and crystallisation ages. Chem. Geol. 482, 101–112. https://doi.org/10.1016/j.chemgeo.2018.02.009.
Snyder, G.A., Neal, C.R., Taylor, L.A., Halliday, A.N., 1997. Anatexis of lunar cumulate mantle in time and space: clues from trace-element, strontium, and neodymium isotopic chemistry of parental Apollo 12 basalts. Geochim. Cosmochim. Acta 61, 2731–2747. https://doi.org/10.1016/S0016-7037(97)00082-3.
Soderblom, L.A., 1970. A model for small-impact erosion applied to the lunar surface. J. Geophys. Res. 75, 2655–2661. https://doi.org/10.1029/JB075i014p02655.
Staid, M.I., et al., 2011. The mineralogy of late stage lunar volcanism as observed by the Moon Mineralogy Mapper on Chandrayaan-1. J. Geophys. Res. 116. https://doi.org/10.1029/2010JE003735.
Stöffler, D., Ryder, G., 2001. Stratigraphy and isotope ages of lunar geologic units: chronological standard for the inner solar system. Space Sci. Rev. 96, 9–54. https://doi.org/10.1023/a:1011937020193.
Taylor, S.R., et al., 1969. Preliminary chemical analyses of Apollo 11 lunar samples. In: Proceedings of the Apollo 11 Lunar Science Conference, pp. 1627–1635.
Terada, K., Anand, M., Sokol, A.K., Bischoff, A., Sano, Y., 2007. Cryptomare magmatism 4.35 Gyr ago recorded in lunar meteorite Kalahari 009. Nature. 450, 849–U14. https://doi.org/10.1038/nature06356.
Tyrie, A., 1988. Age dating of mare in the lunar crater Tsiolkovsky by crater-counting method. Earth Moon Planet. 42, 245–264. https://doi.org/10.1007/BF00058489.
Varatharajan, I., Srivastava, N., Murty, S.V.S., 2014. Mineralogy of young lunar mare basalts: assessment of temporal and spatial heterogeneity using M^3 data from Chandrayaan-1. Icarus. 236, 56–71. https://doi.org/10.1016/j.icarus.2014.03.045.
Vinogradov, A.P., 1971. Preliminary data on lunar ground brought to Earth by automatic probe "Luna-16". In: Proceedings of the Second Lunar Science Conference, pp. 1–16. Geochimica Cosmochimica Acta. Suppl. 2.
Watters, T.R., Johnson, C.L., 2010. Lunar tectonics. In: Watters, T.R., Schultz, R.A. (Eds.), Planetary Tectonics, pp. 121–182.
Whitford-Stark, J.L., Head, J.W., 1977. The Procellarum volcanic complexes-contrasting styles of volcanism. In: Proceedings of 8th Lunar and Planetary Science Conference, pp. 2705–2724.
Whitten, J., et al., 2011. Lunar mare deposits associated with the Orientale impact basin: New insights into mineralogy, history, mode of emplacement, and relation to Orientale Basin evolution from Moon Mineralogy Mapper (M^3) data from Chandrayaan-1. J. Geophys. Res. Planets 116. https://doi.org/10.1029/2010JE003736.
Wilhelms, D.E., McCauley, J.F., 1971. Geological map of the near side of the Moon. In: United States Geological Survey Map, pp. 1–703.
Wu, B., Huang, J., Li, Y., Wang, Y., Peng, J., 2018. Rock abundance and crater density in the candidate Chang'E-5 landing region on the moon. J. Geophys. Res. Planets. 123, 3256–3272. https://doi.org/10.1029/2018JE005820.

Xie, M., Xiao, Z., Zhang, X., Xu, A., 2020. The provenance of regolith at the Chang'e-5 candidate landing region. J. Geophys. Res. Planets 125. https://doi.org/10.1029/2019JE006112 e2019JE006112.
Yue, Z., et al., 2019. Lunar regolith thickness deduced from concentric craters in the CE-5 landing area. Icarus. 329, 46–54. https://doi.org/10.1016/j.icarus.2019.03.032.
Zeigler, R.A., et al., 2019. The Apollo sample collection: 50 years of solar system insight. Elements. 15, 286–287. https://doi.org/10.2138/gselements.15.4.286.
Zhao, J., Xiao, L., Qiao, L., Glotch, T.D., Huang, Q., 2017. The Mons Rümker volcanic complex of the moon: a candidate landing site for the Chang'E-5 mission. J. Geophys. Res. Planets. 122, 1419–1442. https://doi.org/10.1002/2016je005247.